Heat Transfer and Electroosmotic Flow over Stretching Sheet: A Sensitive Analysis through Response Surface Method

J. Prakash[1], Dharmendra Tripathi[2,*], O. Anwar Bég[3], S. Kuharat[3] and Kh. S. Mekheimer[4]

[1] Department of Mathematics, Avvaiyar Government College for Women (Affiliated to Pondicherry University), Karaikal, 609602, India

[2] Department of Mathematics, National Institute of Technology Uttarakhand, Srinagar, 246174, India

[3] Multi-Physical Engineering Sciences Group, Dept. Mechanical and Aeronautical Engineering, Corrosion/Coatings Lab, 3-08, SEE Building, Salford University, Manchester, M54WT, UK

[4] Mathematics Department, Faculty of Science, Al-Azhar University, Nasr City, Cairo, 11884, Egypt

INFORMATION

Keywords:
Factorial plot
response surface methodology (RSM)
electroosmosis
coating flows
stretching sheet
heat transfer

DOI: 10.23967/j.rimni.2025.10.71581

SCIPEDIA
Revista Internacional de Métodos Numéricos para Cálculo y Diseño en Ingeniería
Revista Internacional Métodos numéricos para cálculo y diseño en ingeniería
RIMNI
in cooperation with CIMNE

Heat Transfer and Electroosmotic Flow over Stretching Sheet: A Sensitive Analysis through Response Surface Method

J. Prakash[1], Dharmendra Tripathi[2,*], O. Anwar Bég[3], S. Kuharat[3] and Kh. S. Mekheimer[4]

[1]Department of Mathematics, Avvaiyar Government College for Women (Affiliated to Pondicherry University), Karaikal, 609602, India

[2]Department of Mathematics, National Institute of Technology Uttarakhand, Srinagar, 246174, India

[3]Multi-Physical Engineering Sciences Group, Dept. Mechanical and Aeronautical Engineering, Corrosion/Coatings Lab, 3-08, SEE Building, Salford University, Manchester, M54WT, UK

[4]Mathematics Department, Faculty of Science, Al-Azhar University, Nasr City, Cairo, 11884, Egypt

ABSTRACT

Recent advancements in electro-osmotic surface coatings have led to significant theoretical and numerical exploration of how zeta potential influences the electroosmotic flow of viscous ionic fluids over a stretching sheet. The governing boundary layer equations are derived from the fundamental laws of mass, momentum, and energy conservation using appropriate similarity transformations and non-dimensionalization techniques. This system of equations is solved numerically using MATLAB's *bvp4c* solver. The accuracy of the computational results is confirmed through comparison with previously published studies. To better understand the influence of various parameters on flow and thermal behavior, Response Surface Methodology and Factorial Plot analysis are applied. These statistical tools enable sensitivity analysis by systematically investigating the effects of zeta potential, electroosmosis parameter, electric field strength, and Prandtl number on key flow characteristics such as velocity, temperature distribution, skin friction coefficient, and Nusselt number. The results reveal that the electric field parameter plays a dominant role in enhancing axial velocity and increasing skin friction, making it a key factor in flow dynamics. The zeta potential significantly influences the boundary layer by modifying the electrical double layer and surface charge distribution, leading to noticeable deceleration. Meanwhile, the Prandtl number primarily governs thermal gradients and heat transfer rates, controlling the thermal behavior of the fluid. These physical insights, combined with the optimization capability of Response Surface Methodology, provide actionable guidelines for the design of electroosmotic coating processes and lab-on-chip biomedical devices.

OPEN ACCESS

Received: 07/08/2025

Accepted: 17/10/2025

Published: 03/02/2026

DOI
10.23967/j.rimni.2025.10.71581

Keywords:
Factorial plot
response surface methodology (RSM)
electroosmosis
coating flows
stretching sheet
heat transfer

*Correspondence: Dharmendra Tripathi (dtripathi@nituk.ac.in).

1 Introduction

Fluid flow over a stretching sheet represents a core problem in fluid dynamics, with extensive applications in engineering and industrial processes such as polymer extrusion, glass fiber production, and metal forming. This scenario involves a flat surface that is continuously extended (or in the opposite case, contracted) in one or more directions, inducing flow in the surrounding fluid. Understanding the behavior of such flows is crucial in various fields, including aerospace engineering, manufacturing processes, biological coating manufacture and environmental sciences. The interaction between the stretching surface and the fluid can introduce complex phenomena such as boundary layer separation, momentum re-distribution, heat and mass transfer modification, which are of significant interest both theoretically and for practical applications such as coating in materials processing systems. Numerous researchers have explored transport phenomena from stretching sheets under various external body forces, considering both Newtonian and non-Newtonian (polymeric) fluids. In addition, many types of stretching have been examined including linear wall stretching, quadratic, power-law, exponential etc, all of which have various benefits in industrial manufacturing processes. Crane [1] was the first to analyze boundary layer flow induced by a linearly stretching sheet. Further extending this work, Kumaran and Ramanaiah [2] investigated viscous flow over a quadratically stretching sheet with linear mass flux and presented the associated streamline patterns. Vajravelu and Cannon [3] analyzed viscous flow from a nonlinear stretching sheet using Schauder's fixed point theory, addressing the general case of a power-law stretching velocity. They derived analytical solutions and validated these for the linear stretching case with a Runge-Kutta method. In many coating dynamics processes, heat transfer may also arise. Heat transfer refers to the exchange of thermal energy between systems or objects driven by a temperature gradient. In the context of a stretching sheet, it involves the transfer of heat from the deforming surface to the adjacent fluid. The interaction between the stretching sheet and the fluid, results in convective heat transfer, where thermal energy is transferred through the movement of fluid particles. Frequently the stretching material may also be non-Newtonian, electromagnetic and indeed exhibit combinations of these features as for example in functional polymers, smart biopolymers etc. Ishak [4] numerically investigated the influence of radiative heat flux on thermal convection boundary layer flow of an Eringen micropolar fluid over a linearly stretching sheet. Fang et al. [5] studied boundary layer flow over a continuously stretching sheet with variable thickness, considering a power-law stretching surface velocity. Rana et al. [6] employed a variational finite element method to analyze the transient hydromagnetic nanofluid coating flow over a rotating and quadratically stretching sheet. Hassanien et al. [7] analyzed boundary layer flow and heat transfer of a rheological power-law fluid over a linearly stretching sheet with variable wall temperature, utilizing Chebyshev spectral numerical methods. Siddheshwar and Mahabaleswar [8] analytically investigated thermo-magneto-viscoelastic flow from a stretching sheet in the presence of radiative heat flux. Jat and Chaudhary [9] studied steady two-dimensional laminar stagnation-point boundary layer flow of a Newtonian magnetized viscous fluid. Salleh et al. [10] explored steady boundary layer flow and heat transfer over a stretching sheet with Newtonian heating using a finite-difference method, highlighting the notable effects of the Prandtl number and conjugate parameter on heat transfer behavior. Hayat et al. [11] applied the Liao Homotopy Analysis Method (HAM) to solve MHD flow with heat transfer over a permeable stretching sheet incorporating slip, suction, and thermal radiation. Cortell [12] numerically examined radiative-convective boundary layer flow over a stretching surface. Sreedevi et al. [13] analyzed chemically reactive, time-dependent MHD thermosolutal boundary layer flow of hybrid nanofluids over a stretching sheet, considering wall suction, slip, and thermal radiation using finite-element techniques. Chakrabarti and Gupta [14] investigated hydromagnetic Newtonian flow with heat transfer over a quadratically stretching surface. Andersson [15] derived exact similarity solutions

for viscous flow along a stretching sheet under a transverse magnetic field. Pop and Na [16] computed MHD flow of a Newtonian fluid over a porous stretching surface under strong suction and injection conditions. Fang et al. [17] provided analytical solutions for MHD flow over a permeable stretching surface with hydrodynamic slip and wall suction/injection, demonstrating significant changes in velocity and shear stress profiles under these influences. Furthermore, Gnaneswara Reddy et al. [18] on viscous dissipation and wall slip in non-Newtonian radiative polymer flow from a curved surface; Shahid et al. [19] on thermo-viscoplastic flow over a quadratically stretching sheet with thermal relaxation and radiation; and Tazin et al. [20] on ferromagnetic nanofluid dynamics from a power-law stretching sheet under electromagnetic induction. Collectively, these studies highlight those significant variations in coating flow characteristics such as wall shear stress, Nusselt number, and Sherwood number can be achieved by tuning the stretching behavior alongside other physical effects.

Electro-kinetic coating dynamics play a pivotal role in modern manufacturing, particularly in the development and application of advanced coatings that enhance product performance and durability. Incorporating a comprehensive understanding of electrokinetic coating dynamics into the manufacturing process not only improves coating quality and efficiency, but also reduces material waste and production costs. Electro-kinetics encompasses the study of electrically induced mechanical motion in charged particles or fluids, focusing on the behavior of electrolytes and ionic liquids [21]. In the case of weakly conducting dielectric liquids, this domain is referred to as electro-hydrodynamics (EHD) [22]. A significant subset of electrokinetic phenomena is electro-osmotic flow (EOF) [23], which arises when an applied electric potential drives fluid motion in systems exhibiting a net charge imbalance typically due to charged channel walls. Electroosmotic flow over a stretching sheet enables controlled deposition of ionic fluids using an electric field, an approach particularly useful in emerging microfluidic and biomedical applications. Compared to magnetic manipulation, electric fields offer better precision and efficiency when handling small fluid volumes. As the sheet deforms, the interaction between the fluid and applied electric field induces electroosmotic motion, making this mechanism effective for mass transport and flow control. Recent advancements in electro-osmotic coating processes include works by Yang et al. [24] on biopolymer synthesis via electrophoresis, Konášová et al. [25] on tunable electroosmotic flow using cationic polymer coatings, and Kasicka et al. [26] on fused-silica capillary coatings. Other notable studies include Horvath and Dolník [27] on electrokinetic polymer wall coatings, Huhn et al. [28] on capillary electrophoresis-mass spectrometry coatings, Leclercq et al. [29] on polyelectrolyte multilayers for protein analysis, Sola and Chiari [30] on multifunctional polymeric coatings with adjustable zeta potential, and Sun et al. [31] on pH-independent EOF in anionic polymer-coated capillaries. Theoretical and numerical investigations have also enriched the understanding of EOF. Prakash and Tripathi [32] analyzed electric double layer (EDL) effects in peristaltic pumping of Phan-Thien-Tanner fluids in microchannels, while Balaji et al. [33] modeled ionic electro-osmotic magneto-tribological fluid flow between rotating disks. Misra and Sinha [34] examined EOF in non-Newtonian flows within hydrophobic microchannels, incorporating velocity slip and temperature jump conditions. Zhang et al. [35] investigated Darcy-Forchheimer flow of Casson viscoplastic nanofluids over a stretching sheet under electroosmotic effects, computing flow profiles and wall shear characteristics. Hafez et al. [36] analyzed Casson nanofluid flow with electroosmosis from a stretching surface in a nonlinear porous medium, highlighting that stronger electric parameters, Forchheimer numbers, and permeability lead to greater flow resistance and elevated temperatures due to viscous and Joule heating.

In recent years, there has been a growing emphasis on the use of optimization techniques to enhance thermal and overall system performance. Among these, Response Surface Methodology (RSM) and factorial plot design have gained significant attention. Box and Behnken [37] introduced

innovative three-level experimental designs tailored for quantitative variables, particularly focusing on incomplete factorial designs suitable for estimating second-order polynomial coefficients. This framework has since been widely adopted, with many researchers employing experimental factorial design strategies supported by practical, software-based approaches [38,39]. RSM is particularly effective for conducting sensitivity analysis. In this approach, selected control variables, termed RSM parameters, are evaluated at three coded levels: low (–1), medium (0), and high (+1). RSM facilitates a systematic exploration of the relationships between independent variables (factors) and dependent variables (responses), allowing for the development of quadratic regression models. These models are typically analyzed using statistical software to estimate the influence of each parameter on transport characteristics such as the Nusselt number. The statistical validity of the RSM models is assessed using Analysis of Variance (ANOVA), with significance determined based on p-values at specified confidence levels. Several recent studies have demonstrated the effectiveness of RSM in optimizing thermal and flow-related phenomena. Ahmad et al. [40] applied RSM to enhance membrane performance via thermal-mechanical stretching. Venkatadri et al. [41] combined the D2Q9-based Lattice Boltzmann Method with RSM-based sensitivity analysis to optimize natural convection of a hydromagnetic TiO_2/Cu–water hybrid nanofluid in a fuel cell enclosure containing a porous medium. Their findings indicated that optimal thermal performance occurs at high Darcy number, low nanoparticle concentration, and low Hartmann number. Qader et al. [42] employed RSM along with ANSYS FLUENT to optimize thermal and thermo-hydraulic performance parameters (THPP) in turbulent convection within a solar air heater (SAH) equipped with inclined fins. The RSM analysis identified optimal design configurations fin length of 1.52 mm, fin pitch of 19.04 mm, slant angle of 49°, and Reynolds number of 18,243.5, yielding a maximum THPP of 1.928. Similarly, Mehmood et al. [43] utilized RSM to optimize swirling nanofluid disk coating flows with autocatalytic reactions and entropy generation. Comprehensive discussions on RSM applications across engineering disciplines are provided in the works of Khuri and Mukhopadhyay [44], while Giovanni [45] elaborates on its use in manufacturing and product synthesis. Babu et al. [46] investigated the squeezed flow of a polyethylene glycol and water-based hybrid nanofluid over a magnetized sensor surface, using a statistical approach to analyze heat and mass transfer characteristics. Yusuf et al. [47] focused on optimizing heat transfer in MWCNT-Al2O3 hybrid nanofluids, considering both convective and irreversible effects, highlighting strategies to enhance thermal performance in complex nanofluid systems.

While Response Surface Methodology (RSM) has been previously applied in fluid mechanics and heat transfer optimization, prior electroosmotic studies have largely focused on parametric sweeps or simplified design-of-experiments approaches. To the best of our knowledge, this is the first work to integrate RSM with factorial plots in the context of electroosmotic stretching sheet flows. This combination enables not only the optimization of flow and thermal responses but also the identification of parameter interactions between zeta potential, electroosmosis parameter, electric field, and Prandtl number insights not explicitly addressed in earlier studies. By linking statistical optimization with physical mechanisms such as charge distribution, velocity retardation, and thermal gradient control, this work advances beyond prior EOF-RSM studies and provides a more comprehensive optimization framework for electrokinetic coating processes. In the present study, inspired by electro-osmotic coating dynamics in manufacturing processes, a mathematical model is developed to investigate the influence of zeta potential on the electroosmotic flow of a viscous ionic coating fluid over a stretching surface. The governing equations for mass, momentum, and energy conservation, along with the associated boundary conditions, are non-dimensionalized and reduced to a nonlinear system of coupled ordinary differential equations. This boundary value problem is solved

numerically using the bvp4c solver in MATLAB, with validation against previous studies included to ensure accuracy. The resulting velocity and temperature profiles are further analyzed using Response Surface Methodology (RSM) and Factorial Plots (FP). RSM is demonstrated as a robust tool for sensitivity analysis, enabling optimization of key flow and thermal characteristics namely velocity, temperature, skin friction coefficient, and Nusselt number by systematically varying the zeta potential, electroosmosis parameter, electric field parameter, and Prandtl number. Comprehensive visualization of the flow field is also provided through streamline and isotherm contour plots, offering detailed insights into hydrodynamic and thermal behavior.

Although earlier electroosmotic coating studies have primarily focused on direct analytical or numerical treatments, they often lacked systematic optimization frameworks for exploring parameter interactions. The present work advances this field by integrating Response Surface Methodology (RSM) and factorial analysis into the modeling of electroosmotic stretching sheet flows. This dual approach not only enables sensitivity analysis across key governing parameters but also identifies optimal operating regimes with reduced computational expense. To the best of our knowledge, such integration of optimization tools into electroosmotic stretching sheet studies has not been reported previously, thereby filling an important methodological gap in coating and microfluidic transport research.

2 Mathematical Model

2.1 Problem Definition

The present model considers steady, incompressible, two-dimensional electroosmotic flow of a viscous Newtonian ionic fluid along a stretching sheet coinciding with the plane $y = 0$, with the boundary layer developing in the region $y > 0$. The wall is stretched by applying two equal and opposite forces along the x-axis, keeping the origin fixed. The physical model is depicted in Fig. 1a. In the present formulation, Joule heating and viscous dissipation effects have been neglected. This assumption is valid for moderate electric field strengths (up to order 10^3–10^4 V/m) and ionic concentrations typical of microfluidic applications, where heat generation due to electric current remains small relative to convective and conductive heat transfer. Similarly, viscous dissipation effects are negligible when the electrokinetic Reynolds number is small, as is common in microscale coating flows. For stronger electric fields or highly viscous media, these effects may become significant and should be incorporated into extended models. Thus, the present model is most applicable to microfluidic and thin-film coating systems operating under moderate field intensities and laminar regimes.

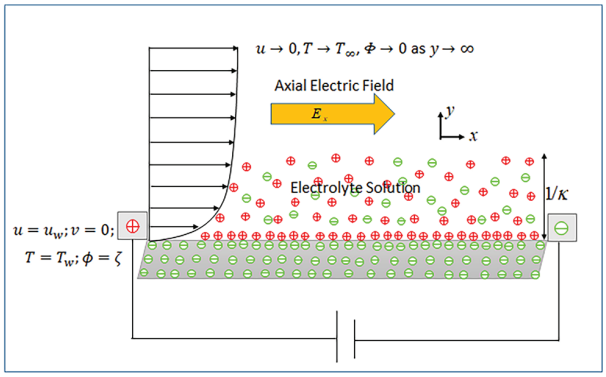

(a)

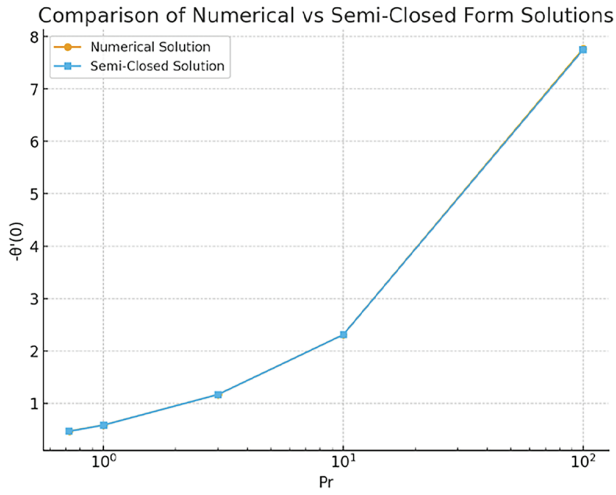

(b)

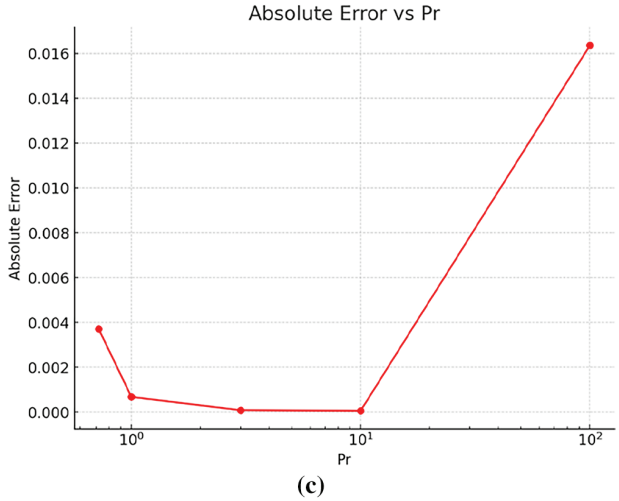

(c)

Figure 1: (Continued)

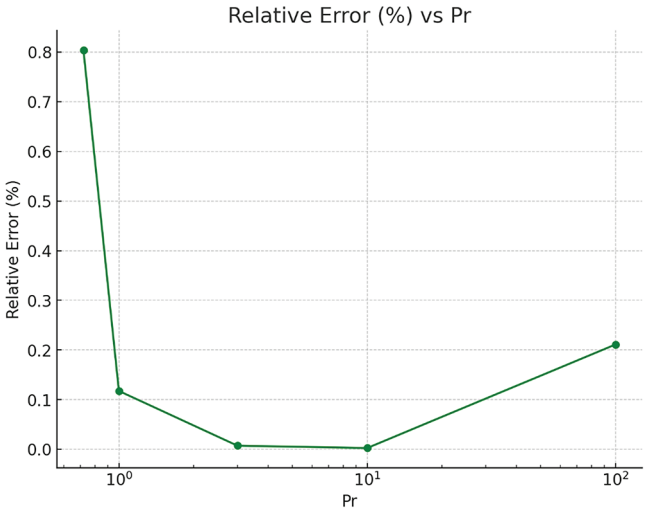

(d)

Figure 1: (**a**): Physical model for electroosmotic boundary layer flow from a stretching sheet, (**b**) Comparison of numerical vs. semi closed form solutions in the absence of U_e *and* γ. (**c**): Absolute error vs. Pr. (**d**): Relative error (%) vs. Pr

2.2 Governing Equations

The flow is considered laminar with constant fluid properties such as viscosity and thermal conductivity, while surface reactions are neglected. Heat conduction follows Fourier's parabolic law. By extending the models in [14–17] and incorporating suitable electrical body force terms [35,36], the boundary layer equations for steady flow and heat transfer can be formulated as:

$$\frac{\partial u}{\partial x} + \frac{\partial v}{\partial y} = 0, \tag{1}$$

$$\rho\left(u\frac{\partial u}{\partial x} + v\frac{\partial u}{\partial y}\right) = \mu\frac{\partial^2 u}{\partial y^2} + \rho_e E_x, \tag{2}$$

$$\rho C_p\left(u\frac{\partial T}{\partial x} + v\frac{\partial T}{\partial y}\right) = \sigma\frac{\partial^2 T}{\partial y^2}. \tag{3}$$

Here, u and v denote the velocity components in the x and y directions, respectively. T is the temperature, μ is the viscosity, ρ is the fluid density, E_x is axially applied electric field, σ is the ionic fluid thermal conductivity, and C_p is the specific heat at constant pressure.

2.3 Electro-Osmotic Flow

The electrostatic potential Φ, which is related to the local net charge density per unit volume ρ_e at specific locations within the ionic fluid (electrolytic solution) through the Poisson equation, represented as [32,33]:

$$\frac{d^2\Phi}{dy^2} = -\frac{\rho_e}{\varepsilon}. \tag{4}$$

Here, ε represents the permittivity (or dielectric constant) of the ionic (electrolytic) fluid. Assuming the validity of the equilibrium Boltzmann distribution, the number concentration of type-i ions, denoted as n_i, in a symmetric electrolyte solution is given by:

$$n_i = n_{i0} exp\left(-\frac{z_i e\Phi}{k_B T_v}\right). \tag{5}$$

Here, n_{i0} and z_i denote the bulk ionic concentration and the valence of type-i ions, respectively, e is the elementary charge, k_B is the Boltzmann constant and T_v is the absolute temperature. For a symmetric electrolyte with valence z, the net volume charge density ρ_e is determined by the total concentration difference between the cations and anions, expressed as:

$$\rho_e = ze(n_+ - n_-). \tag{6}$$

By substituting the expressions for the number concentration of each ion from Eq. (5) into Eq. (6), we obtain:

$$\rho_e = -2zen_0 \sinh\left(\frac{ze\Phi}{k_B T_v}\right). \tag{7}$$

Substituting the expression for charge density from Eq. (7) into the Poisson equation (Eq. (4)) yields:

$$\frac{d^2\Phi}{dy^2} = \frac{2zen_0}{\varepsilon} \sinh\left(\frac{ze\Phi}{k_B T_v}\right). \tag{8}$$

2.4 Boundary Conditions

The boundary conditions reflect the physical reality of the stretching sheet and electroosmotic interface. At the wall ($y = 0$), the no-slip condition is modified to incorporate electroosmotic slip, governed by the zeta potential, which specifies the induced velocity at the charged interface. The wall temperature is prescribed to represent controlled thermal input during coating or lab-on-chip operation. At $y \to \infty$, the velocity is assumed to vanish, reflecting quiescent fluid beyond the electrokinetic influence region, while the temperature approaches ambient conditions. These conditions ensure that the model realistically captures both near-wall electrokinetic effects and the asymptotic decay of flow and thermal disturbances in the bulk fluid.

$$u = ax = u_w, v = 0, T = T_w, \Phi = \zeta \text{ at } y = 0, \tag{9a}$$

$$u \to 0, T \to T_\infty, \Phi \to 0 \text{ as } y \to \infty. \tag{9b}$$

2.5 Non-Dimensional Transformations

To simplify the system of partial differential equations into ordinary differential equations, the following similarity transformations are applied:

$$\eta = y\sqrt{\frac{a}{\nu}}, u = axf'(\eta), v = -\sqrt{a\nu}f(\eta), \theta(\eta) = \frac{T - T_\infty}{T_w - T_\infty}, \psi = \frac{ze\Phi}{k_b T_v}. \tag{10}$$

Here, a prime indicates differentiation with respect to the dimensionless transverse coordinate η, and ν represents the kinematic viscosity of the ionic liquid. By substituting the above scaling variables from Eq. (10) into Eqs. (1), (3), and (8), along with the boundary conditions in Eq. (4), the following nonlinear ordinary differential equations governing momentum, energy, and electric potential are obtained:

$$f''' + ff'' - (f')^2 + U_e\psi'' = 0, \tag{11}$$

$$\theta'' + Prf\theta' = 0, \tag{12}$$

$$\psi'' - m^2 \sinh(\psi) = 0. \tag{13}$$

The dimensionless boundary conditions take the following form:

$$f' = 1,\ f = 0, \theta = 1 \ and\ \psi = \gamma \ at\ \eta = 0, \tag{14}$$

$$f' \to 0; \theta \to 0 \ and\ \psi \to 0 \ as\ \eta \to \infty. \tag{15}$$

Here, f represents the dimensionless stream function, $\theta(\eta)$ is non-dimensional temperature function, ψ denotes the electrical potential. The Prandtl number is given by $\Pr = \mu C_p/\sigma$, while $U_e = \frac{1}{ax} U_{HS}$ defines the electric field parameter, where $U_{HS} = -\frac{K_B T_v \varepsilon E_x}{\mu z e}$ is the Helmholtz–Smoluchowski velocity. The zeta potential parameter is expressed as $\gamma = \frac{ze\zeta}{K_B T_v}$ and the electroosmosis parameter is defined by $m^2 = \kappa^2 \frac{v}{a}$, where $\kappa^2 = -\frac{2z^2 e^2 n_0}{\varepsilon K_B T_v}$ is the Debye–Hückel parameter. The reciprocal of κ, i.e., $\frac{1}{\kappa}$ denotes the Debye length, which characterizes the thickness of the electric double layer (EDL). Zeta potential plays a pivotal role in assessing the stability of ionic liquids. It reflects the electrostatic interactions either repulsive or attractive between dispersed droplets within the fluid. Thus, it serves as a measure of the electrokinetic potential and indicates the surface charge in colloidal systems. Importantly, the stability of an ionic (electrolyte colloidal) liquid system is governed by the interplay between opposing forces: the van der Waals attractions and the repulsive forces of the electrical double layer.

Important surface characteristics in electro-osmotic materials processing are defined by shear stress $\left(C_f\right)$ (skin friction coefficient) and Nusselt number (Nu) (heat transfer coefficient) at the surface of the sheet:

$$C_f = \frac{\tau_w}{\rho u_w^2} \ and\ Nu = -\frac{x q_w}{\sigma\left(T_w - T_\infty\right)}. \tag{16}$$

In the above-mentioned expressions, dimensional shear stress τ_w and heat flux at the wall, q_w are respectively:

$$\tau_w = \mu \left(\frac{\partial u}{\partial y}\right)\Big|_{y=0} \ and\ q_w = -\sigma \left(\frac{\partial T}{\partial y}\right)\Big|_{y=0}. \tag{17}$$

Making use of (10) and (16) in (17), the non-dimensional form of (16) emerges as:

$$\sqrt{Re_x} C_f = f''(0). \tag{18}$$

Furthermore, the local wall heat transfer gradient is defined as:

$$\sqrt{Re_x} Nu = \theta'(0), \tag{19}$$

where $Re_x = \frac{av}{u_w^2}$ denotes the local Reynolds number, C_{fx} represents the coefficient of skin friction and Nu indicates the Nusselt number.

3 Numerical Solution

The boundary value problem defined by Eqs. (11)–(15) is of seventh order. Due to the strong coupling, nonlinearity, and presence of higher-degree terms, obtaining an analytical solution is extremely challenging, but not impossible. Therefore, the governing Eqs. (11)–(13), along with the boundary conditions (14) and (15), are solved numerically using MATLAB's bvp4c algorithm. To facilitate and accelerate this numerical solution, the following steps were implemented:

- System Reduction: The original set of higher-order partial differential equations was simplified by adding additional variables, resulting in a set of first-order ordinary differential equations.
- Boundary conditions were created to ensure that the newly added variables adhered to the restrictions of the issue.
- The first estimates for these new variables were obtained, serving as a foundation for the numerical solution.
- The required solution was reached by following these processes and efficiently solving the resultant problem using the bvp4c function.

To utilize the bvp4c solver, the nonlinear ordinary differential equations and associated boundary conditions must be converted into a system of first-order differential equations. The standard syntax used is: sol = bvp4c (@OdeBVP, @OdeBC, solinit). Here, @OdeBVP defines the system of first-order ODEs, @OdeBC specifies the boundary conditions, and solinit contains the initial mesh points and initial guesses for the solution at these points. To obtain multiple solutions, different initial guesses can be provided in solinit. The reformulated first-order system is expressed as follows:

$$f = F(1)\,;\, f' = F(2)\,;\, f'' = F(3)\,;\, f''' = F'(3)\,;\, \theta = F(4)\,;\, \theta' = F(5)\,;\, \theta'' = F'(5)\,; \tag{20}$$

$$\psi = F(6)\,;\, \psi' = F(7)\,;\, \psi'' = F'(7)\,; \tag{21}$$

here:

$$F'(3) = F(2)^2 - F(1)\,F(3) - U_e m^2 \sinh(F(6))\,, F'(5) = -PrF(1)\,F(5), \tag{22}$$

$$F'(7) = m^2 \sinh(F(6))\,. \tag{23}$$

It is the desire for achieving a continuous solution that gives the mesh selection and error function a critical role. After reaching its starting value of 10^{-9}, the discrepancy remained the same. At a value of η equal to seven, the numerical solution is accurate and asymptotically convergent. The numerical solution was calculated on a grid that had 197 different individual elements. A residual of 8.402×10^{-11} is the highest value computed.

The bvp4c solver was employed with absolute and relative tolerance levels of 10^{-9}. Convergence was verified through grid independence tests by refining mesh points until further refinement produced changes of less than 0.1% in the output quantities. Additionally, sensitivity tests with multiple sets of initial guesses confirmed the stability of the obtained solutions. These checks ensure the robustness of the numerical results and minimize dependence on arbitrary solver initialization.

4 Optimization Procedure and Validation

4.1 Response Surface Methodology (RSM)

Quantitative data and rigorous testing are very efficient methods for describing several variables concurrently while minimising resource use. In the approach known as Response Surface Methodology

(RSM) [44,45], a number of different aspects and variables that have an effect on the response variable are taken into consideration. The RSM approach features the following steps:

(i) Developing and analysing tests to meet the necessary and reliable standards for the intended outcome.
(ii) Utilizing mathematical models that accurately represent the response surfaces of first and second orders with the highest level of accuracy.
(iii) Identifying the optimal combination of factors that provide the highest or lowest response surface.
(iv) Examining the direct and interaction impacts of the method parameters using ANOVA (Analysis of Variance).

However, there are other objectives that may be accomplished by using RSM statistical design:

(i) Computing the coefficients of a quadratic regression model.
(ii) Decreasing the quantity of tests.
(iii) Conducting the analysis of the impact of many variables on test outcomes.
(iv) Offering the absence of the fit test.
(v) Determining the optimal values of the components via a minimal number of experiments.
(vi) Also, computing the factorial plot and streamline plot with help of the RSM data.

4.2 Method for Testing

The present study examines the impact of three key factors (U_e, m and γ) on velocity and skin friction coefficient, as well as the impact of four key parameters (U_e, m, γ and Pr) on temperature and Nusselt number. This investigation is conducted utilising the statistical RSM model. RSM is therefore used to determine the optimal configuration of parameters in computing findings within a certain topic of study. Furthermore, it included the interplay among the aforementioned factors [37,44,45].

According to the preliminary testing conducted for this research, the following is a range of modifications that may be made to the model parameters:

(i) Electric field parameter ($-5 \leq U_e \leq 5$),
(ii) Electroosmosis parameter ($0 \leq m \leq 4$),
(iii) Zeta potential ($0 \leq \gamma \leq 1$), and
(iv) Prandtl number ($3 \leq Pr \leq 9$).

The selection of these parameters occurs at three distinct levels. Additionally, the determination of the statistical model table, which consists of 20 or 31 runs, is dependent on the number of parameters and their corresponding levels. A model is constructed for each dependent variable using the Response Surface Methodology (RSM) technique. This model comprehensively captures the main effects of variables on each variable, as well as the interplay between these factors on each variable independently. A potential depiction of the multivariate model is described in more detail in Box and Behnken [37] and Gardiner and Gettinby [39]. A model is developed for each dependent variable using the RSM approach. This model captures the primary impacts of variables on each variable as well as the interaction effects of those factors on each variable individually. One possible representation of the

multivariate model is following [37,39] of the form:

$$Y = \alpha_0 + \sum_{i=1}^{n} \alpha_{ii} x_i x_i + \sum_{i=1}^{n} \sum_{j=i+1}^{n} \alpha_{ij} x_i x_j. \tag{24}$$

The equation consists of many regression coefficients. n represents the number of independent variables, α_0 represents the intercept, α_i represents the linear regression coefficient for the i^{th} factor, α_{ii} represents the quadratic regression coefficient for the i^{th} factor, and α_{ij} represents the interaction between the i^{th} and j^{th} factors. Y represents the dependent variable. The objective is to enhance the efficiency of the response of variable Y and establish an accurate correlation between the independent variables and the response variable. Also, n denotes the quantity of independent variables. In this model, the value of n is set to 20 for velocity and skin friction coefficient, and 31 for temperature and Nusselt number.

A summary of the parameters and their levels is presented in in Tables 1 and 2 for axial velocity (AV), skin friction coefficient (SFC), temperature and Nusselt number (NN). In that order, the low level is (−1), the middle level is (0), and the high level is (+1). The quadratic polynomial regression equations are statistically analyzed using specialized software to identify significant coefficients and assess the influence of various parameters on the dependent variables. The factors and answers were examined using an experimental methodology, with coded values representing the replies. The first step in making a 95% confident decision about the findings' fitting quality is to employ a *certain coefficient of determination* and *adjust resources based on the p-value*. An analysis of variance (ANOVA), factorial plots and streamlines are then used to examine the replies.

Table 1: Impact of key parameter involved in axial velocity (AV) and skin friction coefficient (SFC) for fixed value at $\eta = 1$

U_e	m	γ	f'	f''
0	1.5	0.5	0.367690822965314	−1.000172536480670
0	1.5	0.5	0.367690822965314	−1.000172536480670
0	1.5	1.3409	0.367690822965314	−1.000172536480670
0	4.02269	0.5	0.367690717672249	−1.000172542009050
0	1.5	0.5	0.367690822965314	−1.000172536480670
−3	0	1	0.367690822965314	−1.000172536480670
0	1.5	0.5	0.367690822965314	−1.000172536480670
3	3	0	0.367690789711274	−1.000172449262650
−5.0454	1.5	0.5	−0.432578205727882	−3.509972731546970
5.04538	1.5	0.5	−0.432578205727882	−3.509972731546970
−3	3	1	−0.552774695416748	−8.259961426095960
−3	3	0	0.367691299536369	−1.000171916443280
0	1.5	0.5	0.367690822965314	−1.000172536480670
−3	0	0	0.367690822965314	−1.000172536480670
0	1.5	−0.3409	0.367690822965314	−1.000172536480670

(Continued)

Table 1 (continued)

U_e	m	γ	f'	f''
3	0	0	0.367690822965314	−1.000172536480670
3	0	1	0.367690822965314	−1.000172536480670
0	1.5	0.5	0.367690822965314	−1.000172536480670
0	−1.0227	0.5	0.367690822965314	−1.000172536480670
3	3	1	0.859192738012697	5.211187554981360

Table 2: Impact of key parameter involved in temperature and Nusselt number (NN) for fixed value $\eta = 0.6$

U_e	m	γ	Pr	θ (0.6)	θ' (0)
−1	0	1	3	0.3965448897617420	−1.1651646653947300
1	3	1	3	0.3093455632899180	−1.3733138635440100
0	1.5	0.5	5	0.2568913610509200	−1.5679885416314600
2	1.5	0.5	5	0.2090389952381750	−1.7045369712799600
1	0	1	7	0.1723629331608260	−1.8953442626318700
1	0	0	7	0.1723629331608260	−1.8953442626318700
0	1.5	0.5	5	0.2568913610509200	−1.5679885416314600
0	1.5	−0.5	5	0.2568913610509200	−1.5679885416314600
0	1.5	0.5	5	0.2568913610509200	−1.5679885416314600
0	1.5	0.5	5	0.2568913610509200	−1.5679885416314600
−1	0	0	7	0.1723629331608260	−1.8953442626318700
−1	0	1	7	0.1723629331608260	−1.8953442626318700
0	1.5	0.5	5	0.2568913610509200	−1.5679885416314600
0	1.5	0.5	5	0.2568913610509200	−1.5679885416314600
−1	3	0	7	0.1723629331216680	−1.8953442627215000
0	1.5	1.5	5	0.2568913618658070	−1.5679885393672100
0	1.5	0.5	9	0.1179606358324630	−2.1783344519344900
1	3	1	7	0.1100748432028430	−2.1531142187498100
1	0	1	3	0.3965448897617420	−1.1651646653947300
0	−1.5	0.5	5	0.2568913610509200	−1.5679885416314600
1	0	0	3	0.3965448897617420	−1.1651646653947300
−1	3	0	3	0.3965448928662200	−1.1651646620200100
0	1.5	0.5	5	0.2568913610509200	−1.5679885416314600
−1	3	1	7	0.4114503611839500	−1.2537784554036500
0	1.5	0.5	1	0.6677783051604480	−0.5826632579114160
−2	1.5	0.5	5	0.1641203121043650	−1.7168166454245400
−1	3	1	3	0.7208303996921570	−0.5196591760604450
1	3	0	7	0.1723629331204580	−1.8953442627243300
0	4.5	0.5	5	0.2568913615231520	−1.5679885358492900

(Continued)

Table 2 (continued)

U_e	m	γ	Pr	θ (0.6)	θ' (0)
1	3	0	3	0.3965448898363880	−1.1651646628048200
−1	0	0	3	0.3965448897617420	−1.1651646653947300

4.3 Validation

The methodology section outlines the use of the BVP4C numerical tool in MATLAB for solving the coupled non-linear differential equations. It is critical to provide detailed information on the model validation process in order to strengthen its validity. The manuscript should specifically detail the comparison between the results from the bvp4c tool and existing data from previous studies. For validation, it is critical to specify the sources of existing literature data, including details such as data collection conditions and parameters. Table 3 displays the numerical results obtained by simulating the current model using the bvp4c solver. The changes in Nusselt number are examined in relation to the variations in Prandtl number (Pr) for a specific situation where $U_e = \gamma = 0$. These results are then compared to the findings provided by Hassanien et al. [7]. The great degree of agreement demonstrates the validity of the current flow model analysis and numerical simulations. Also, Table 3 clearly demonstrates that the data show a high level of compliance.

Table 3: Numerical solution based on Eqs. (11)–(13) without U_e and γ compared to known findings Hassanien et al. [7]

Pr	Present numerical solution for $-\theta'(0)$	Existing semi-closed form solution (Hassanien et al. [7]) for $-\theta'(0)$
0.72	0.466972501154412	0.46325
1	0.582663261619192	0.58198
3	1.165164660051621	1.16525
10	2.307950035497639	2.30801
100	7.765610856461937	7.74925

Fig. 1b shows a direct comparison between the present numerical solution and the existing semi-closed form solution across various Prandtl numbers (Pr). Both methods produce results that align extremely closely, as the curves practically overlap across all values of Pr. At low Pr values (e.g., 0.72 and 1), the numerical and semi-closed values are nearly identical, while at higher Pr values (e.g., 100), although the magnitude of the results increases significantly, the two solutions continue to follow each other closely. This indicates that both approaches are consistent and reliable for estimating the heat transfer parameter $\theta'(0)$, with very small deviations.

The second graph (Fig. 1c) illustrates the absolute error between the numerical and semi-closed solutions as a function of Pr. The error remains extremely small for most Pr values, lying close to zero across the scale. At intermediate values (Pr = 3 and 10), the error is almost negligible (on the order of 10^{-4}), while the maximum error occurs at the highest Pr value (Pr = 100), where it reaches about 0.016. This demonstrates that the discrepancy between the two methods is minimal throughout but slightly

grows with increasing Pr, suggesting that at very large Pr, the semi-closed approximation begins to deviate slightly from the numerical benchmark.

Fig. 1d presents the relative error in percentage terms, offering a clearer sense of proportional deviation. The relative error is highest at the lowest Pr (0.72) at approximately 0.80%, showing that even small absolute differences can appear larger in relative terms when the magnitude of the solution is small. As Pr increases, the relative error rapidly decreases, falling below 0.2% for $\mathrm{Pr} = 100$. This confirms that the two solutions are in excellent agreement across all cases, with relative discrepancies that are practically negligible in engineering or scientific contexts. Overall, the relative error trend emphasizes that both methods are consistent, and the semi-closed form is a highly reliable approximation of the numerical solution.

5 Results and Discussion

This section examines how the electric field parameter, electroosmosis parameter, and zeta potential affect the velocity and skin friction coefficient. An optimal mode is achieved, and a sensitivity analysis is conducted on the influential factors of velocity and SFC (skin friction coefficient) in relation to the strength of electric fields. This study therefore aims to accomplish optimized electro-kinetic stretching, of relevance to emerging multi-functional materials processing.

The present work introduces the novel integration of Response Surface Methodology (RSM) and factorial analysis into the study of electroosmotic stretching sheet flows. Unlike previous electroosmotic coating studies, which primarily emphasize direct analytical or numerical solutions, our approach leverages statistical optimization tools to identify key parameter interactions, predict system performance with reduced computational demand, and propose optimal operating regimes. This methodological advancement not only broadens the analytical scope of electroosmotic flows but also provides a more robust framework for engineering design and application. The present analysis focuses on four key physical parameters that govern electroosmotic stretching sheet flows:

(i) **Zeta potential (ζ):** a measure of the surface charge at the solid–liquid interface, which determines the strength and thickness of the electrical double layer (EDL). Variations in ζ directly influence the electroosmotic body force and, consequently, the velocity distribution within the boundary layer.

(ii) **Electroosmosis parameter (K):** representing the coupling between electrokinetic forces and viscous resistance. This parameter quantifies the contribution of electroosmotic driving forces to the overall flow dynamics.

(iii) **Electric field strength (E):** denoting the magnitude of the applied external field, which acts as a primary driving mechanism for ionic fluid motion. Physically, stronger electric fields intensify fluid acceleration and modify surface shear, directly impacting coating uniformity.

(iv) **Prandtl number (Pr):** the ratio of momentum diffusivity to thermal diffusivity, which dictates the relative thickness of velocity and thermal boundary layers. Higher Pr values correspond to lower thermal diffusivity, thereby steepening temperature gradients and enhancing convective heat transfer. Together, these parameters capture the coupled electrokinetic, viscous, and thermal mechanisms that control coating performance and microfluidic transport.

5.1 Analysis of Variance (ANOVA)

The analysis of variance (ANOVA) is a statistical tool that gives variance to discover correlations that are statistically significant between two or more input elements. Using the statistical instrument

known as MINITAB-19, the values of the regression model for twenty different runs are analysed and shown in Tables 4–15. Using the analysis of variance (ANOVA) and the sequential f-test, these findings were produced. All the statistical estimators that were generated via the use of the ANOVA approach are shown in Tables 4–15. Both the momentum Eq. (11) and energy Eq. (12) have their own F-values and p-values, respectively. To determining the variance of the data, the F-value is used. An F-value larger than one validates the accuracy of the data. Validating regression models is another use of the p-value that may be employed. In the process of creating the equation of output responses, the p value that is less than 0.05 is regarded as statistically significant; however, the p value that is larger than 0.05 will disappear and will not be taken into consideration.

Table 4: Coded coefficients for AV

Term	Coef	SE coef	T-value	p-value	VIF
Constant	0.3603	0.0947	3.80	0.003	
U_e	0.174	0.106	1.65	0.131	1.00
m	−0.053	0.106	−0.50	0.628	1.00
γ	−0.053	0.106	−0.50	0.628	1.00
U_e^2	−0.663	0.173	−3.83	0.003	1.02
m^2	0.137	0.173	0.79	0.447	1.02
γ^2	0.137	0.173	0.79	0.447	1.02
$U_e m$	0.499	0.232	2.15	0.057	1.00
$U_e \gamma$	0.499	0.232	2.15	0.057	1.00
$m\gamma$	−0.152	0.232	−0.65	0.528	1.00

Table 5: Analysis of variance for AV

Source	DF	Adj SS	Adj MS	F-value	p-value	Significant
Model	9	1.62431	0.180479	3.35	0.037	YES
Linear	3	0.17293	0.057644	1.07	0.406	NO
U_e	1	0.14598	0.145983	2.71	0.131	NO
m	1	0.01347	0.013474	0.25	0.628	NO
γ	1	0.01347	0.013474	0.25	0.628	NO
Square	3	0.92997	0.309990	5.75	0.015	YES
U_e^2	1	0.79279	0.792792	14.70	0.003	YES
m^2	1	0.03375	0.033747	0.63	0.447	NO
γ^2	1	0.03375	0.033747	0.63	0.447	NO
2-way interaction	3	0.52141	0.173805	3.22	0.070	YES
$U_e m$	1	0.24921	0.249206	4.62	0.051	YES
$U_e \gamma$	1	0.24921	0.249207	4.62	0.051	YES
$m\gamma$	1	0.02300	0.023001	0.43	0.528	NO
Error	10	0.53943	0.053943			
Lack-of-Fit	5	0.53943	0.107887	*	*	

(Continued)

Table 5 (continued)

Source	DF	Adj SS	Adj MS	F-value	*p*-value	Significant
Pure error	5	0.00000	0.000000			
Total	19	2.16375				

Note: $R^2 = 75.07\%$; Adjected $R^2 = 52.63\%$; *Not applicable.

Table 6: Fits and diagnostics for unusual observations for AV

Obs	AV	Fit	Resid	Std Resid
10	−0.433	−0.129	−0.303	−2.08R
16	0.368	−0.018	0.386	2.89R
20	0.859	0.562	0.297	2.22R

Note: R: Large residual.

Table 7: Coded coefficients value for skin friction coefficient (SFC)

Term	Coef	SE Coef	T-value	*p*-value	VIF	Correlation
Constant	−1.025	0.752	−1.36	0.203		
U_e	0.986	0.499	1.98	0.076	1.00	Not correlated
m	−0.077	0.499	−0.15	0.881	1.00	Not correlated
γ	−0.077	0.499	−0.15	0.881	1.00	Not correlated
U_e^2	−0.728	0.486	−1.50	0.165	1.02	Moderately correlated
m^2	0.160	0.486	0.33	0.749	1.02	Moderately correlated
γ^2	0.160	0.486	0.33	0.749	1.02	Moderately correlated
$U_e m$	1.684	0.652	2.58	0.027	1.00	Not correlated
$U_e \gamma$	1.684	0.652	2.58	0.027	1.00	Not correlated
$m\gamma$	−0.131	0.652	−0.20	0.845	1.00	Not correlated

Table 8: Analysis of variance for SFC

Source	DF	Adj SS	Adj MS	F-value	*p*-value	Significant
Model	9	68.022	7.5580	2.22	0.011	YES
Linear	3	13.449	4.4830	1.32	0.323	NO
U_e	1	13.288	13.2880	3.91	0.076	NO
m	1	0.080	0.0805	0.02	0.881	NO
γ	1	0.080	0.0805	0.02	0.881	NO
Square	3	9.068	3.0226	0.89	0.480	NO
U_e^2	1	7.633	7.6325	2.24	0.165	NO
m^2	1	0.367	0.3671	0.11	0.749	NO

(Continued)

Table 8 (continued)

Source	DF	Adj SS	Adj MS	F-value	*p*-value	Significant
$\boldsymbol{\gamma^2}$	1	0.367	0.3671	0.11	0.749	NO
2-way interaction	3	45.505	15.1685	4.46	0.031	YES
$\boldsymbol{U_e m}$	1	22.684	22.6840	6.67	0.027	YES
$\boldsymbol{U_e \gamma}$	1	22.684	22.6840	6.67	0.027	YES
$\boldsymbol{m\gamma}$	1	0.137	0.1374	0.04	0.845	NO
Error	10	34.021	3.4021			
Lack-of-fit	5	34.021	6.8041	*	*	
Pure error	5	0.000	0.0000			
Total	19	102.043				

Note: $R^2 = 66.66\%$; Adjected $R^2 = 36.65\%$; *Not applicable.

Table 9: Fits and diagnostics for unusual observations for SFC

Obs	SFC	Fit	Resid	Std Resid
11	−8.26	−6.07	−2.19	−2.06R
16	−1.00	−3.79	2.79	2.63R
20	5.21	2.64	2.57	2.43R

Note: R: Large residual.

Table 10: Coded coefficients for temperature

Term	Coef	SE coef	T-value	*p*-value	VIF	Correlation
Constant	0.2569	0.0246	10.44	0.000		
U_e	−0.0260	0.0133	−1.95	0.068	1.00	Not correlated
m	0.0172	0.0133	1.30	0.213	1.00	Not correlated
γ	0.0172	0.0133	1.30	0.213	1.00	Not correlated
Pr	−0.1231	0.0133	−9.26	0.000	1.00	Not correlated
U_e^2	−0.0114	0.0122	−0.94	0.363	1.03	Moderately correlated
m^2	0.0062	0.0122	0.51	0.619	1.03	Moderately correlated
γ^2	0.0062	0.0122	0.51	0.619	1.03	Moderately correlated
Pr^2	0.0402	0.0122	3.30	0.005	1.03	Moderately correlated
$U_e m$	−0.0446	0.0163	−2.74	0.015	1.00	Not correlated
$U_e \gamma$	−0.0446	0.0163	−2.74	0.015	1.00	Not correlated
$U_e Pr$	0.0069	0.0163	0.42	0.678	1.00	Not correlated
$m\gamma$	0.0259	0.0163	1.59	0.131	1.00	Not correlated
mPr	−0.0038	0.0163	−0.23	0.820	1.00	Not correlated
γPr	−0.0038	0.0163	−0.23	0.820	1.00	Not correlated

Table 11: Analysis of variance for temperature

Source	DF	Adj SS	Adj MS	F-value	*p*-value	Significant
Model	14	0.523186	0.037370	8.82	0.000	YES
Linear	4	0.393883	0.098471	23.24	0.000	YES
U_e	1	0.016173	0.016173	3.82	0.068	NO
m	1	0.007138	0.007138	1.68	0.213	NO
γ	1	0.007138	0.007138	1.68	0.213	NO
Pr	1	0.363435	0.363435	85.78	0.000	YES
Square	4	0.053863	0.013466	3.18	0.042	NO
U_e^2	1	0.003722	0.003722	0.88	0.363	NO
m^2	1	0.001088	0.001088	0.26	0.619	NO
γ^2	1	0.001088	0.001088	0.26	0.619	NO
Pr^2	1	0.046128	0.046128	10.89	0.005	YES
2-way interaction	6	0.075440	0.012573	2.97	0.038	YES
$U_e m$	1	0.031761	0.031761	7.50	0.015	YES
$U_e \gamma$	1	0.031761	0.031761	7.50	0.015	YES
$U_e Pr$	1	0.000758	0.000758	0.18	0.678	NO
$m\gamma$	1	0.010706	0.010706	2.53	0.131	NO
mPr	1	0.000227	0.000227	0.05	0.820	NO
γPr	1	0.000227	0.000227	0.05	0.820	NO
Error	16	0.067789	0.004237			
Lack-of-fit	10	0.067789	0.006779	*	*	
Pure error	6	0.000000	0.000000			
Total	30	0.590974				

Note: $R^2 = 88.53\%$; Adjected $R^2 = 78.49\%$; *Not applicable.

Table 12: Fits and diagnostics for unusual observations for temperature

Obs	T	Fit	Resid	Std Resid
26	0.1641	0.2632	−0.0991	−2.36R
27	0.7208	0.6109	0.1099	2.62R

Note: R: Large residual.

Table 13: Coded coefficients for nusselt number

Term	Coef	SE coef	T-value	*p*-value	VIF	Correlation
Constant	−1.5680	0.0539	−29.08	0.000		
U_e	−0.0720	0.0291	−2.47	0.025	1.00	Not correlated
m	0.0342	0.0291	1.17	0.257	1.00	Not correlated

(Continued)

Table 13 (continued)

Term	Coef	SE coef	T-value	*p*-value	VIF	Correlation
γ	0.0342	0.0291	1.17	0.257	1.00	Not correlated
Pr	−0.3786	0.0291	−13.00	0.000	1.00	Not correlated
U_e^2	−0.0227	0.0267	−0.85	0.407	1.03	Moderately correlated
m^2	0.0130	0.0267	0.49	0.633	1.03	Moderately correlated
γ^2	0.0130	0.0267	0.49	0.633	1.03	Moderately correlated
Pr^2	0.0598	0.0267	2.24	0.039	1.03	Moderately correlated
$U_e m$	−0.1096	0.0357	−3.07	0.007	1.00	Not correlated
$U_e \gamma$	−0.1096	0.0357	−3.07	0.007	1.00	Not correlated
$U_e Pr$	−0.0029	0.0357	−0.08	0.937	1.00	Not correlated
$m\gamma$	0.0513	0.0357	1.44	0.169	1.00	Not correlated
mPr	−0.0033	0.0357	−0.09	0.926	1.00	Not correlated
γPr	−0.0033	0.0357	−0.09	0.926	1.00	Not correlated

Table 14: Analysis of variance for nusselt number

Source	DF	Adj SS	Adj MS	F-value	*p*-value	Significant
Model	14	4.17909	0.29851	14.67	0.000	YES
Linear	4	3.62073	0.90518	44.47	0.000	YES
U_e	1	0.12448	0.12448	6.12	0.025	YES
m	1	0.02810	0.02810	1.38	0.257	NO
γ	1	0.02810	0.02810	1.38	0.257	NO
Pr	1	3.44007	3.44007	169.01	0.000	YES
Square	4	0.13160	0.03290	1.62	0.219	NO
U_e^2	1	0.01473	0.01473	0.72	0.407	NO
m^2	1	0.00481	0.00481	0.24	0.633	NO
γ^2	1	0.00481	0.00481	0.24	0.633	NO
Pr^2	1	0.10243	0.10243	5.03	0.039	YES
2-way interaction	6	0.42675	0.07113	3.49	0.021	YES
$U_e m$	1	0.19206	0.19206	9.44	0.007	YES
$U_e \gamma$	1	0.19206	0.19206	9.44	0.007	YES
$U_e Pr$	1	0.00013	0.00013	0.01	0.937	NO
$m\gamma$	1	0.04214	0.04214	2.07	0.169	NO
mPr	1	0.00018	0.00018	0.01	0.926	NO
γPr	1	0.00018	0.00018	0.01	0.926	NO
Error	16	0.32567	0.02035			
Lack-of-fit	10	0.32567	0.03257	*	*	
Pure error	6	0.00000	0.00000			
Total	30	4.50476				

Note: $R^2 = 92.77\%$; Adjected $R^2 = 86.44\%$; *Not applicable.

Table 15: Fits and diagnostics for unusual observations for nusselt number

Obs	Nu	Fit	Resid	Std Resid
24	−1.2538	−1.4764	0.2227	2.42R
26	−1.7168	−1.5147	−0.2021	−2.19R
27	−0.5197	−0.7116	0.1919	2.08R

Note: R: Large residual.

Typically, the factorial design (FD), central composite design (CCD), and Box-Behnken design (BBD) are used for constructing second-order empirical correlations. Out of the three designs, the BBD needs a somewhat smaller number of numerical tests to extract all the necessary information on the answers. BBD also refrains from conducting numerical trials in harsh settings. Thus, in this work, the BBD (Box-Behnken Design) is used to optimise the velocity and skin friction coefficient in the stretching sheet (f(1) and f′(0)). This optimisation is achieved by considering *three important physical parameters*: the electric field parameter (U_e), the electroosmosis parameter (m) and the zeta potential parameter (γ). These three parameters were selected at three *distinct levels (low, moderate, and high)*, and the experimental design (based on Box-Behnken design (BBD)), along with their related answers, is shown in Tables 4–15.

While the RSM and ANOVA analyses provide valuable insights, certain limitations must be acknowledged. For example, the adjusted R^2 value for the skin friction coefficient (SFC) model is relatively low (36.65%), indicating limited predictive reliability. This is consistent with the high sensitivity of SFC to nonlinear interactions among ζ, electroosmosis parameter, and electric field strength, which a quadratic polynomial may not fully capture. Additionally, outliers and large residuals observed in Tables 5, 6, 8 and 9 highlight parameter regions where the statistical approximation diverges from the numerical solution. These deviations, though expected in strongly nonlinear transport systems, restrict the predictive strength of certain models. Accordingly, the claims regarding RSM should be interpreted primarily in terms of identifying dominant parameters and interaction effects, rather than precise quantitative prediction. Future improvements could include transformation techniques or narrowing factor ranges to enhance regression quality.

In uncoded units, the regression equation for the axial velocity and temperature equations at $\eta = 1$ may be expressed as:

$$f' = 0.466 - 0.0832U_e - 0.0.5m - 0.149\gamma - 0.02606U_e^2 + 0.0215m^2 + 0.194\gamma^2 + 0.0392U_e m + 0.1177U_e\gamma - 0.071m\gamma. \quad (25)$$

The constant parameters U_e, m *and* γ coefficients in Eq. (25) have a clear negative value, indicating their critical role in reducing axial velocity profiles. Fig. 2a–c depicts the numerical solution (obtained using the MATLAB bvp4c method) for the axial velocity profile. This solution exactly corresponds to the features described in Eq. (25). The factorial plot discusses the interaction between the parameters. Fig. 2a–c shows the impact of the electric field parameter (U_e), electroosmosis parameter (m) and zeta potential parameter (γ) on both axial velocity (f') and axial displacement (f) profiles. The x-axis represents a dimensionless spatial coordinate (η), while the y-axis indicates the values of f' and f. For Axial Velocity (f') Profiles: (i) As $U_e, m,$ and γ increases, the peak axial velocity generally decreases. This suggests that a stronger electric field tends to inhibit the maximum fluid velocity. (ii) The shape of the velocity profiles changes with $U_e, m,$ and γ. For lower $U_e, m,$ and γ values, the profiles are more

parabolic, indicating a predominant shear-driven flow. As $U_e, m,$ and γ increases, the profiles become flatter, suggesting a greater influence of the electric field on the flow. The axial displacement increases with $U_e, m,$ and γ. This implies that a stronger electric field leads to a larger net fluid movement in the axial direction. The curvature of the displacement profiles also changes with $U_e, m,$ and γ. A higher $U_e, m,$ and γ results in a steeper initial rise in displacement, indicating a quicker response of the fluid to the electric field.

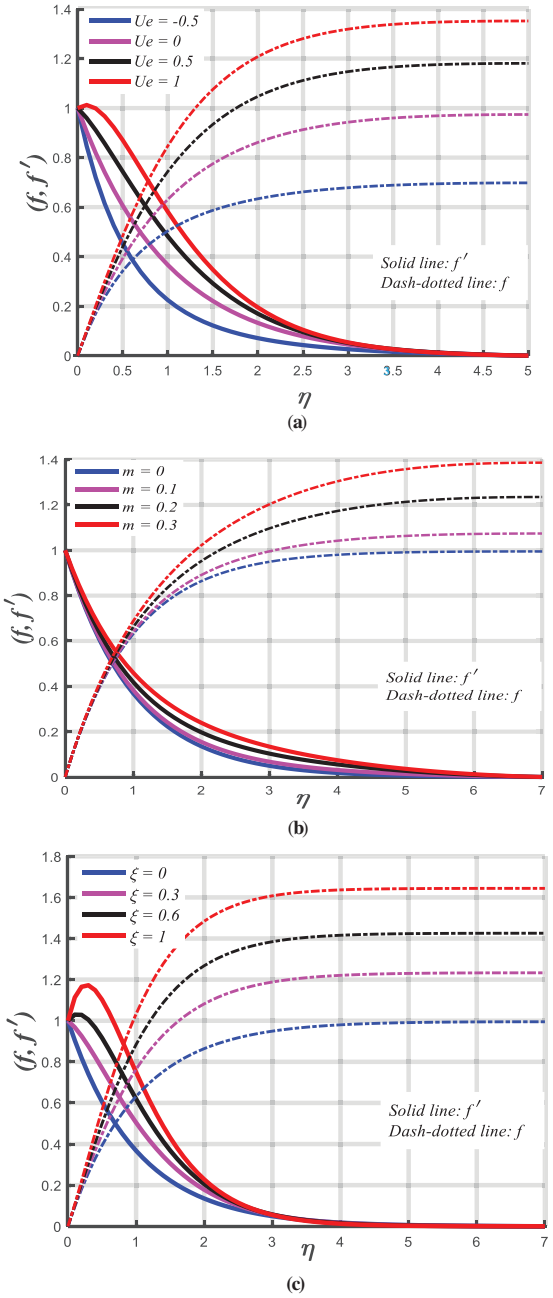

Figure 2: (**a**): Axial displacement and velocity profiles for U_e. (**b**): Axial displacement and velocity profiles for m. (**c**): Axial displacement and velocity profiles for γ

In uncoded units, the regression equation for the temperature equations at $\eta = 1$ may be expressed as:

$$\theta = 0.8004 + 0.0459U_e - 0.0077m - 0.023\gamma - 0.1582Pr - 0.0114U_e^2 + 0.00274m^2 + 0.0247\gamma^2 + 0.01004Pr^2 - 0.0297U_em - 0.0891U_e\gamma + 0.00344U_ePr + 0.0345m\gamma - 0.00126mPr - 0.0038\gamma Pr. \quad (26)$$

The equation for regression in uncoded units for the skin friction coefficient (SFC) and Nusselt number (Nu) equations is calculated as:

$$SFC = -0.68 - 0.794U_e - 0.177m - 0.53\gamma - 0.0809U_e^2 + 0.071m^2 + 0.64\gamma^2 + 0.374U_em + 1.123U_e\gamma - 0.175m\gamma, \quad (27)$$

$$Nu = -0.255 + 0.154U_e - 0.0231m - 0.069\gamma - 0.3356Pr - 0.0227U_e^2 + 0.0058m^2 + 0.052\gamma + 0.01496Pr^2 - 0.0730U_em - 0.2191U_e\gamma - 0.0014U_ePr + 0.0684m\gamma - 0.0011mPr - 0.0033\gamma Pr. \quad (28)$$

The selected BBD's validity is assessed by a statistical t-test, utilising the p-value, coefficient of determination (R^2), and adjusted R^2 (R^2 *adj*) statistical characteristics. Tables 5, 6, 8, 9, 11, 12, 14 and 15 illustrate an analysis of variance (ANOVA) that includes different statistical parameters for the response variables $f(1), \theta(1)$ and $f'(0), \theta'(0)$. The values of (R^2, Adjusted R^2) for $f(1), \theta(1)$ were determined to be (0.7507, 0.5263) and (0.8853, 0.7847), whereas for $f'(0), \theta'(0)$ they were (0.6666, 0.3665) and (0.9277, 0.8644). A value of R^2 near to 1 indicates the *optimal predicting performance* of the selected model. A further finding from the statistical study was that the p-value and F-value for $f(1), \theta(1)$ were found to be (<0.05, 3.35) and (<0.05, 8.82), whereas the corresponding values for $f'(0), \theta'(0)$ were (<0.05, 2.22) and (<0.05, 14.67). Considering that the p-value should be less than 0.05 for a confidence level of 95% and the F-value should be more than 1, these data suggest that the designs that were chosen are statistically significant.

The ANOVA results highlight clear differences in the relative influence of the governing parameters on fluid flow and heat transfer responses (Tables 10–15). The Prandtl number (Pr) shows the strongest effect on the Nusselt number, confirming that thermal diffusivity dominates heat transfer rates in electroosmotic stretching sheet flows. The electric field parameter (E) significantly influences axial velocity and skin friction, demonstrating its role in enhancing momentum transport through electrokinetic forcing. The zeta potential (ζ) exhibits moderate but non-negligible effects by altering the electrical double layer and charge distribution, thereby modifying near-wall flow deceleration. Finally, the electroosmosis parameter contributes primarily to modifying bulk fluid motion, with smaller but consistent effects compared to Pr and E. Collectively, these results provide not only statistical validation of the model but also practical physical insights: thermal control strategies should prioritize adjustment of Pr, while electrokinetic control can be effectively achieved through tuning E and ζ.

5.2 Factorial and Contour Plots for Axial Velocity

In factorial experiments, Minitab employs a factorial plot to visually depict the impacts of several variables and their interactions. Factorial studies include the simultaneous manipulation of numerous variables to examine their impact on a response variable. There are two main categories of factorial

plots: The plot illustrates the primary effects: (i) Main Effect: The overall influence of modifying a single component on the outcome variable while considering the different amounts of other variables. Every factor's degree corresponds to an average reaction. The x-axis denotes the independent variables, whereas the y-axis indicates the mean value of the dependent variable. If the line is not parallel to the horizontal axis, it shows that the factor has a substantial impact on the response variable. (ii) Interaction Plot: The graphic depicts the connection between two or more variables, demonstrating how their interplay influences the result. An interaction effect refers to the combined impact of many variables on the response variable, which is distinct from the simple addition of their separate effects. An interaction plot displays the average response for different combinations of component values. The x-axis indicates a single variable, whereas distinct lines reflect various degrees of the second variable. Non-parallel lines suggest a correlation or relationship between the components. Fig. 3a–d provide factorial plots and contour plots, respectively, to examine the interaction effects of input variables on axial velocity. Factorial plots are used as graphical instruments to visually represent the impacts of many category variables on a response variable. They assist in comprehending the impact of altering one component level on the response while considering the simultaneous changes in other variables, which is vital for detecting interactions among factors. There are two primary categories of factorial plots (see Fig. 3a,b)—*the main effects plot and the interaction plot*. The *main effects plot* displays the average impact of each factor on the response variable without considering the influence of other variables. It aids in determining if each individual component has a substantial influence on the answer and in which direction (positive or negative). An *interaction plot* visually displays the relationship between two factors and illustrates how the impact of one element varies depending on the degree of the other factor. It helps in determining if the elements collaborate to impact the response in a synergistic or antagonistic manner.

First, the main effects plot is analyzed to evaluate the correlation between the response variable and the predictor variables. The lines are assessed to ascertain the presence of a primary effect, using the following method: When the line is *parallel* to the x-axis, there is *no primary impact*. The response value remains constant, regardless of the value of the predictor. A primary impact is observed when the line is *not horizontal*. The response value exhibits variability across different predictor values. The more pronounced the incline of the line, the larger the size of the primary impact. Fig. 3a shows that the axial velocity is significantly influenced by the electric field parameter, in comparison to the electroosmosis parameter and zeta potential. The electroosmosis parameter and zeta potential parameter exhibit comparable behavior in terms of axial velocity. Fig. 3b displays the interaction plot depicting the estimated average axial velocity as a function of the combinations of $U_e * m$, $U_e * \gamma$ and $m * \gamma$. The observed figure exhibits apparent interaction effects due to the non-parallel lines, indicating that the connection between axial velocity and each element is contingent upon the configuration of another factor. The Analyse Factorial Design findings reveal that the interaction effects for $U_e * m$, $U_e * \gamma$ and $m * \gamma$ are statistically significant. The factorial plots reveal that the combined increase in zeta potential and electric field strength significantly enhances axial velocity. Physically, this arises from the fact that both parameters act on the electrical double layer (EDL): a higher zeta potential increases surface charge density, while a stronger electric field enhances the electroosmotic body force acting on the counter-ions. The interaction thus produces a synergistic acceleration of near-wall fluid, which also elevates surface shear. Conversely, when the Prandtl number interacts with the electroosmosis parameter, the combined effect is seen in thermal transport: while electroosmotic forcing modifies fluid velocity profiles, a higher Prandtl number reduces thermal diffusivity, confining heat near the wall.

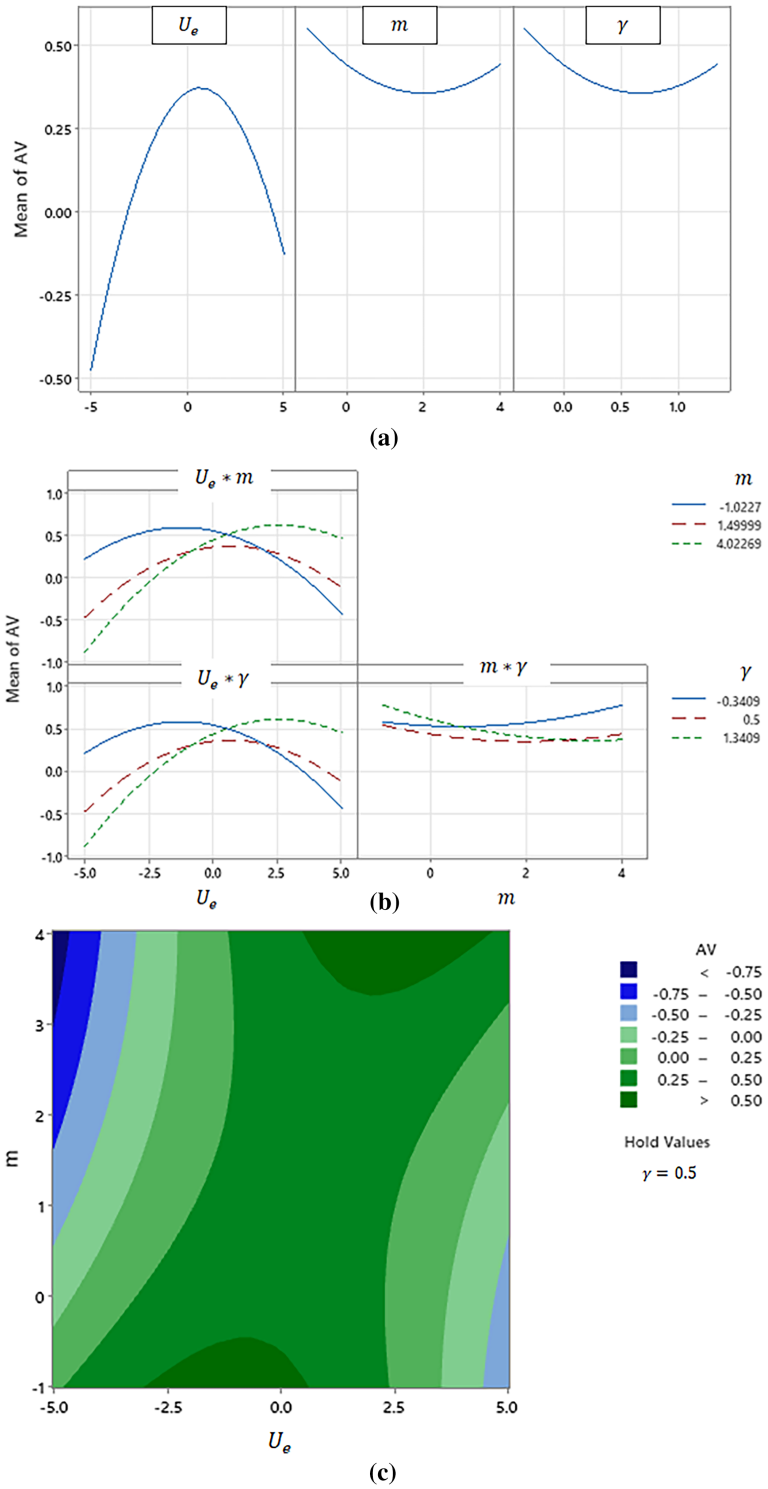

Figure 3: (Continued)

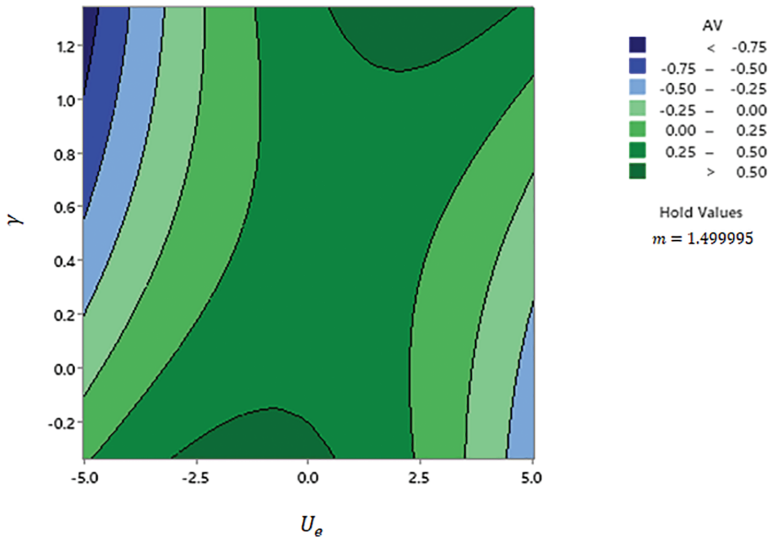

(d)

Figure 3: (**a**) Factorial (main effects) plot for axial velocity (AV). (**b**) Factorial interaction plot for axial velocity (AV). (**c**) Contour plot of axial velocity vs. m, U_e. (**d**) Contour plot of axial velocity vs. U_e, γ

Contour plots in Fig. 3c,d are used to examine the combined impacts of input factors on axial velocity (AV). The curved outlines are a result of the inclusion of statistically significant quadratic factors in the model. The figure shows that the *greatest ratings for wrinkle resistance* of AV are in the top right corner, which indicates high values for both m, U_e and m, γ. The figures show that the *lowest ratings for wrinkle resistance* are in the bottom left corner, indicating low values for both m, U_e and m, γ.

5.3 Factorial and Contour Plots for SFC

Fig. 4a,b shows contour plots that reveal the combined effects of input variables on SFC. Since statistically significant quadratic factors were added to the model, the edges are bent. Fig. 4a illustrates that the sluggish decrease in SFC is seen as the Helmholtz-Smoluchowski U_e increases, whereas the quick decrease is observed as γ increases. It is noteworthy that $U_{HS} = -\dfrac{K_B T_v \varepsilon E_x}{\mu z e}$ and is directly proportional to the axial electrical field, E_x. Clearly a stronger axial electrical field therefore suppresses the skin friction as the electro-osmotic body force, $+U_e\psi''$ in the momentum Eq. (11) opposes momentum development (it is effectively negative for positive E_x values). The zeta potential however arises only in the wall boundary condition, $\psi = \gamma$ in Eq. (14), where $\gamma = \dfrac{ze\zeta}{K_B T_v}$ and therefore when this parameter is elevated, it influences the charge distribution at the boundary (substrate) which produces a more direct impedance to the velocity. The maximum rate of axial velocity is seen at lower values of both U_e and γ when m is at a moderate level. For the electro-osmotic coating, therefore peak acceleration in the boundary layer is achieved with this combination of the three control parameters. Fig. 4b demonstrates that increasing the values of both m and γ leads to a decrease in the skin friction coefficient (SFC), indicating strong deceleration. Since $m^2 = \kappa^2 \dfrac{\nu}{a}$ is the electroosmosis parameter where $\kappa^2 = -\dfrac{2z^2 e^2 n_0}{\varepsilon K_B T_v}$ represents the electroosmotic parameter, while $\dfrac{1}{\kappa}$ denotes the Debye

length (characteristic thickness of the EDL), the implication is that thinner EDL is associated with deceleration whereas a thicker EDL corresponds to acceleration.

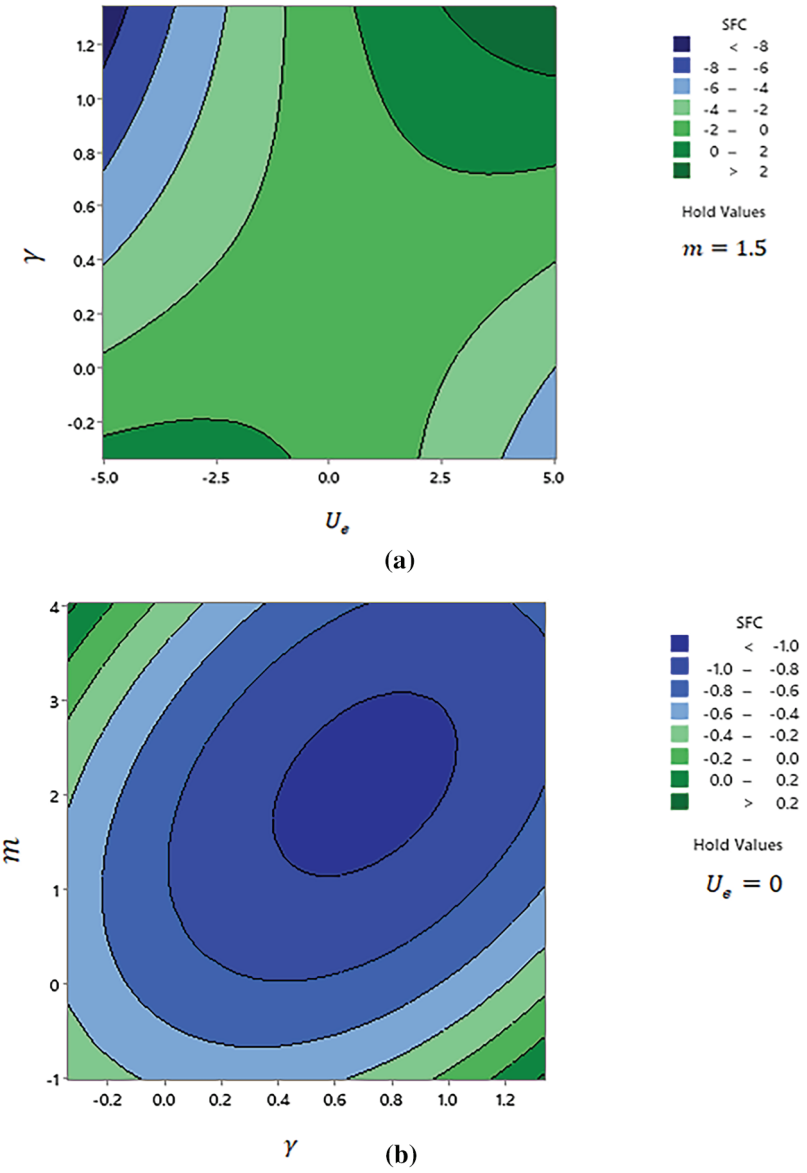

Figure 4: (**a**) Contour plot of axial velocity vs. U_e, γ. (**b**) Contour plot of axial velocity vs. m, γ

5.4 Factorial and Contour Plot for Temperature

The factorial and contour plots presented in Figs. 5a,b and 6a–c, respectively, are utilized to analyze the interaction effects of input variables on temperature. Factorial and contour design is a statistical method used to study the effect of multiple factors (U_e, m, γ, Pr) on a response variable. This approach systematically varies the levels of the input factors to observe their individual and combined effects on the response variable, namely temperature. Fig. 5a represents the factorial main effect on temperature profile in the presence of U_e, m, γ and Pr. The parameters are not aligned

horizontally, resulting in a substantial influence on the temperature profile. Additionally, Prandtl number, Pr, which since it is inversely proportional to thermal conductivity of the ionic liquid (electrolytic solution), has significant influence on temperature, can be compared to the effects of U_e, m *and* γ. The estimated average temperature and its relationship to various combinations of $U_e * m, U_e * \gamma, m * \gamma, U_e * Pr, m * Pr$ and $\gamma * Pr$ are shown in the interaction plot in Fig. 5b. The link between temperature and each element depends on the configuration of another component, as shown by the apparent interaction effects in the observed image caused by the non-parallel lines. Parallel lines in interaction plots signify the absence of interaction, but non-parallel lines show the presence of an interaction effect. The outcomes of the factorial design show that there are statistically significant interaction effects for $U_e * m, U_e * \gamma, m * \gamma, U_e * Pr, m * Pr$ and $\gamma * Pr$. This helps in determining if the variables collaborate to have a synergistic impact on the response. Fig. 5b displays the interaction plot depicting the estimated average temperature as a function of the combinations of $U_e * m, U_e * \gamma, m * \gamma, U_e * Pr, m * Pr$ and $\gamma * Pr$. The observed figure exhibits apparent interaction effects due to the non-parallel lines, indicating that the connection between temperature and each element is contingent upon the configuration of another factor. The Analyse Factorial Design findings reveal that the interaction effects for $U_e * m, U_e * \gamma, m * \gamma, U_e * Pr, m * Pr$ and $\gamma * Pr$ are statistically significant.

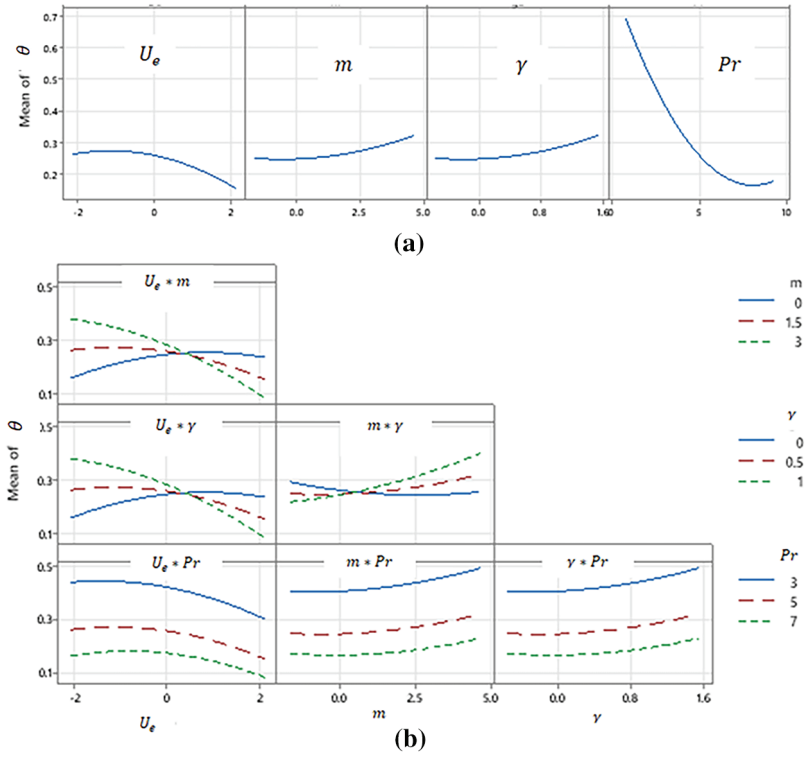

Figure 5: (**a**) Main effects factorial plot for temperature. (**b**) Factorial interaction plot for temperature

A contour plot is a graphical representation used to examine the correlation between a fitted response variable and two continuous predictor variables. It functions by presenting contour lines that link sites with identical anticipated response values. The temperature profile (θ) contour plot is shown in Fig. 6a–c for the pair parameters (U_e, m), (U_e, Pr) and (Pr, m). Fig. 6a illustrates the non-linear relationship between θ and the combined impacts of m and U_e. The greatest temperature, θ, is seen

at high values of m and U_e, while maintaining a fixed value of $Pr = 5$ (representative of aqueous ionic coating fluids) and $\gamma = 0.5$. Furthermore, as shown in Fig. 6b,c, the maximum temperature is computed for low-level values of (U_e, Pr) and (Pr, m) when $\gamma = 0.5$ level.

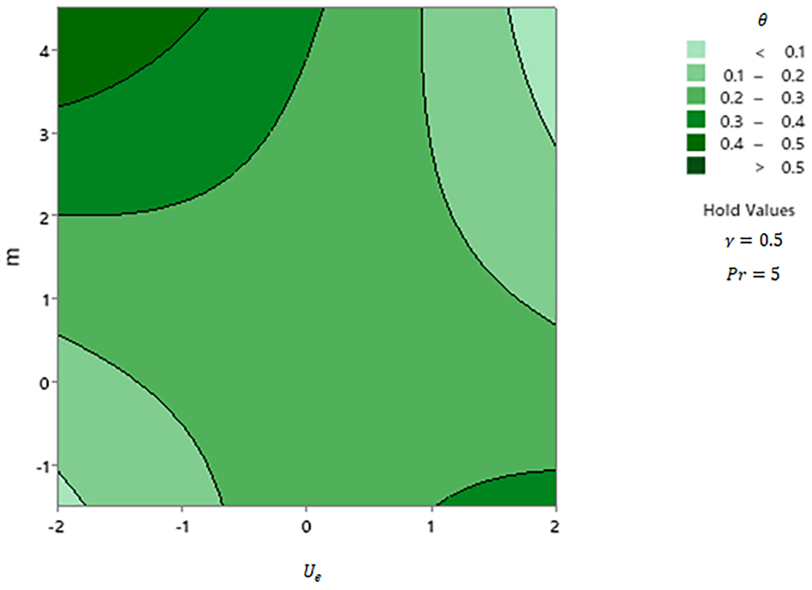

(a)

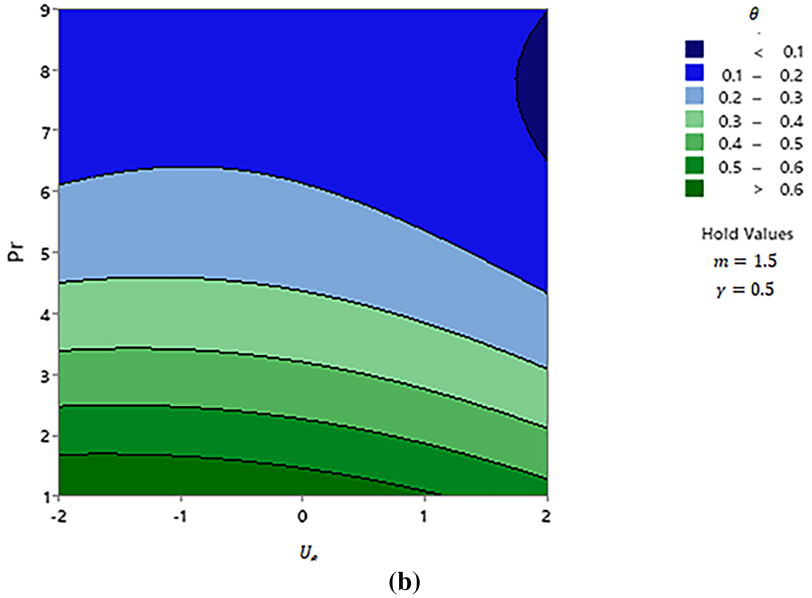

(b)

Figure 6: (Continued)

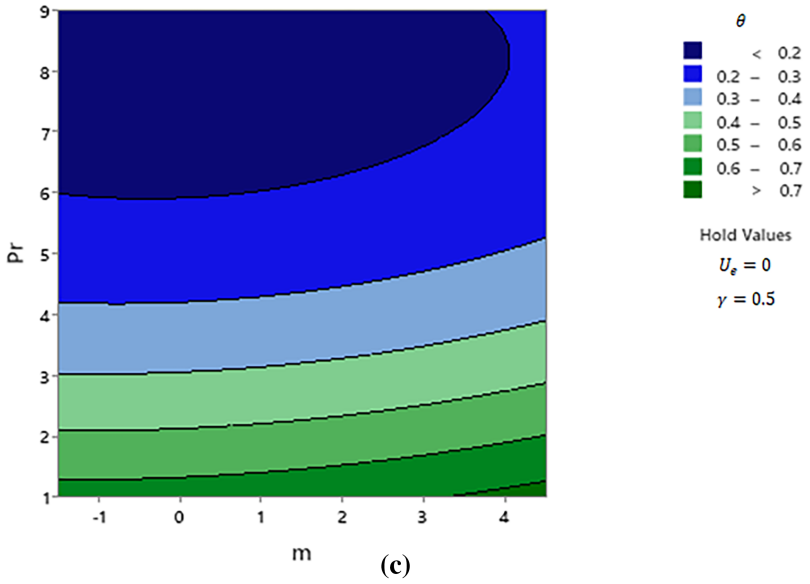

Figure 6: (**a**) Contour plot of temperature vs. U_e, m. (**b**) Contour plot of temperature vs. U_e, Pr. (**c**) Contour plot of temperature vs. m, Pr

5.5 Factorial and Contour Plot for Nusselt Number

Both the factorial plots and the contour plots that are shown in Figs. 7a,b and 8a–c are used to investigate the interaction effects of the input variables on the Nusselt number (Nu). Fig. 7a shows the impact of U_e, m, γ and Pr on the Nusselt number in a factorial main effect model. A significant impact on the temperature profile is caused by the parameters not being horizontally aligned. Furthermore, it has been noted that U_e, m, γ and Pr all significantly affect Nusselt number. The fitted mean of the Nusselt number against combinations of $U_e{*}m$, $U_e{*}\gamma$, $U_e{*}Pr, m{*}Pr, m{*}\gamma$ and $Pr{*}\gamma$ are shown in the interaction plot, as visualized in Fig. 7b. The fact that the lines in this figure are not perfectly parallel suggests that the strength of the correlation between axial velocity and each variable is conditional on the value of some other variable, suggesting the presence of interaction effects. According to the findings of the Analyse Factorial Design, there is a statistically significant interaction effect for $U_e * m$, $U_e * \gamma$, $U_e * Pr, m * Pr, m * \gamma$ and $Pr * \gamma$.

The Nusselt number profile (Nu) contour plot is shown in Fig. 8a–c for the pair parameters (U_e, Pr), (m, Pr) and (Pr, γ). As shown in Fig. 8a–c, the maximum temperature is observed for low-level values of (U_e, Pr), (m, Pr) and (Pr, γ) also the minimum temperature occurred in the high values of (U_e, Pr), (m, Pr) and (Pr, γ). Hence, this analysis provides insight into how various combinations of these variables influence temperature profiles, aiding in understanding heat transfer processes and optimizing thermo-electro-osmotic coating process systems.

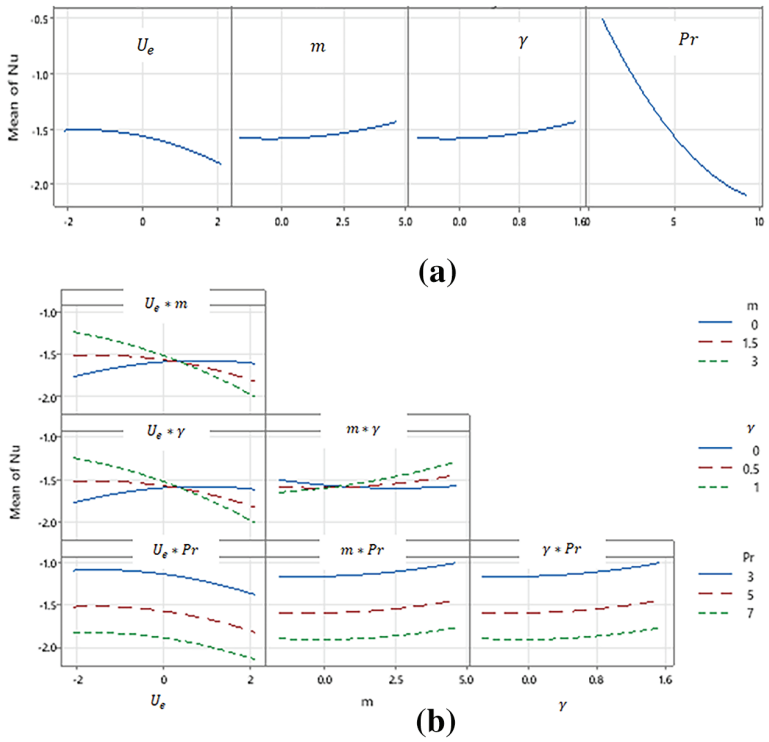

Figure 7: (**a**) Main effects factorial plot for nusselt number. (**b**) Factorial interaction plot for nusselt number

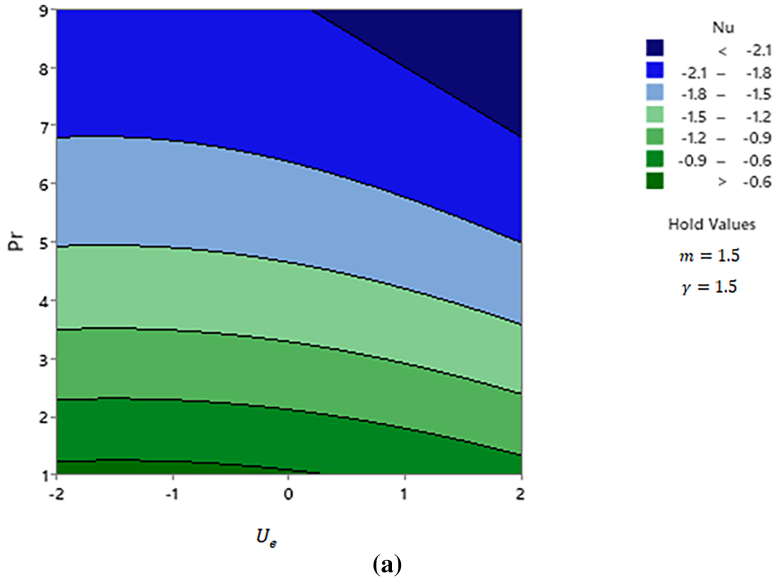

Figure 8: (Continued)

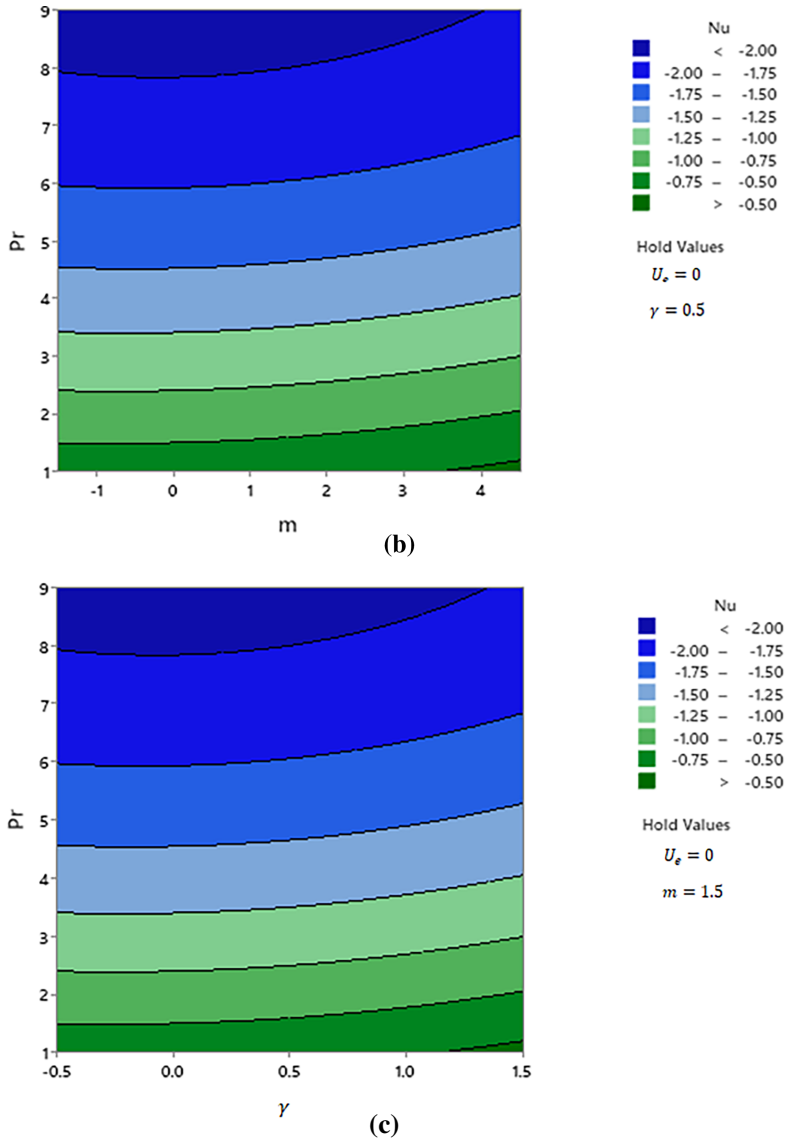

Figure 8: (**a**) Contour plot of Nusselt number vs. U_e, Pr. (**b**) Contour plot of nusselt number vs. m, Pr. (**c**) Contour plot of nusselt number vs. Pr, γ

RSM is overall an excellent tool which has been shown to offer some significant advantages in thermal optimization in electro-osmotic stretching coating flows, which we have summarized below:

- **Prediction between Input and Output Parameters:** Response Surface Methodology plays a crucial role in developing empirical models that capture the relationships between input variables and the corresponding output responses. By systematically varying the input parameters, RSM helps us understand how each factor and their interactions influence the response variables. This predictive capability is essential to our research, enabling a structured and quantitative understanding of the complex dynamics involved in fluid flow and heat transfer.

- **Output Parameter Optimization:** The primary advantage of using RSM is its ability to optimize the response variables within a given range of input parameters. Through the design of experiments and subsequent analysis, RSM identifies the optimal conditions that maximize or minimize the desired outputs. This optimization process is vital for improving the efficiency and overall performance of the systems being investigated. Using RSM, we can determine the best combination of input parameters that yields the most favourable outcomes, such as maximum heat transfer or minimal flow resistance.
- **Novelty and Contribution:** The innovative application of RSM significantly contributes to the novelty of our research. By incorporating RSM into our analysis, we have developed a more comprehensive understanding of the system's behaviour than traditional methods would allow. This methodology not only provides a robust statistical framework for analysing complex interactions but also offers a systematic approach for exploring a wide range of operating conditions. In this context, RSM is instrumental in uncovering new insights and optimizing performance metrics that were previously unattainable.
- The novelty of this study lies in the integration of RSM and factorial plots with the electroosmotic stretching sheet flow model. Unlike prior works that primarily examined flow and thermal responses under fixed parametric conditions, our approach provides a statistically robust optimization framework capable of capturing complex parameter interactions, quantifying significance levels, and predicting optimal performance regimes. This contribution extends beyond descriptive analysis to deliver actionable optimization insights, establishing a methodological advancement over existing electroosmotic coating investigations. In doing so, the study not only deepens theoretical understanding of electrokinetic flows but also equips engineers with practical tools for designing efficient coating and microfluidic systems.

5.6 Applications and Practical Impact

The present analysis extends beyond theoretical modeling and provides practical insights for the design and optimization of advanced coating and microfluidic systems. In biomedical and pharmaceutical coating processes, precise control of electroosmotic flow is essential for achieving uniform surface deposition and functional film formation. Our results highlight that variations in zeta potential typically ranging between -50 and $+50$ mV in realistic systems can strongly influence surface charge distribution and boundary layer retardation, enabling designers to fine-tune coating adhesion and thickness. Similarly, the role of applied electric field strength, often operating within 10^2–10^4 V/m in microfluidic and lab-on-chip devices, was shown to significantly modify axial velocity and skin friction, parameters directly tied to coating uniformity and process efficiency. The sensitivity of thermal gradients to the Prandtl number further suggests pathways for tailoring heat transfer in ionic and polymeric fluids commonly employed in biomedical coatings. These findings are particularly relevant for lab-on-chip technologies, where controlled thermal and mass transport are critical for diagnostics, biosensing, and targeted drug delivery. By integrating Response Surface Methodology (RSM) and factorial analysis, this study delivers actionable optimization guidelines that bridge theoretical electroosmotic flow models with industrial parameter ranges, thereby strengthening the link between fundamental fluid mechanics and real-world engineering applications.

6 Concluding Remarks

To optimize the electro-osmotic coating flows, a mathematical model was developed to simulate the influence of zeta potential on the electroosmotic flow of a viscous ionic coating fluid over a stretching surface. The governing boundary layer equations for mass, momentum, and energy conservation, along with their boundary conditions, were transformed into a dimensionless system of nonlinear coupled ordinary differential equations forming a boundary value problem. This system was solved numerically using the bvp4c solver in MATLAB, with validation performed through comparison with existing studies. Further analysis was carried out using Response Surface Methodology (RSM) and Factorial Plots (FP) to investigate the sensitivity of the flow system to key parameters. RSM effectively mapped the influence of the zeta potential, electroosmosis parameter, electric field parameter, and Prandtl number on primary output characteristics, including velocity, temperature, skin friction coefficient, and Nusselt number. A strong correlation was established between the input variables and output responses through the RSM-based empirical modeling. Analysis of Variance (ANOVA) was also conducted to evaluate regression coefficients and quantify residual errors. The study provides a detailed evaluation of how variations in zeta potential, electroosmosis strength, electric field intensity, and thermal diffusivity impact the fluid flow and heat transfer behavior. The principal computational findings are summarized as follows:

a) Evidence of a robust relationship between inputs and outputs is seen by the higher R_2 and Adj R_2 values for axial velocity, skin friction coefficient, temperature, and Nusselt number.

b) In addition to demonstrating normal data and a strong correlation between input parameters and output responses, the residual plots of AV, SFC, temperature, and Nusselt number further corroborated this.

c) In comparison to other factors, the electric field parameter had a more substantial impact on the axial velocity and skin friction coefficient, whereas the Prandtl number had a more pronounced influence on temperature and the Nusselt number.

d) A stronger axial electrical field was observed to deplete the skin friction, whereas a modification in zeta potential (arising only in the wall boundary condition) influenced the charge distribution at the boundary and a more significant deceleration effect in the boundary layer.

e) A stronger axial electric field enhances the electroosmotic body force, which accelerates near-wall fluid motion and raises surface shear. This explains the observed increases in axial velocity and skin friction.

f) Higher Pr values correspond to lower thermal diffusivity, leading to steeper temperature gradients near the wall. Physically, this results in stronger convective heat transfer and higher Nusselt number.

g) Changes in surface charge density alter the structure of the electrical double layer (EDL), directly influencing the balance between electrostatic driving forces and viscous resistance. This manifests as measurable deceleration effects within the boundary layer.

h) The interplay of electrokinetic driving forces, viscous stresses, and thermal diffusion governs coating uniformity and heat transfer in electroosmotic systems, providing a mechanistic foundation for optimization through RSM.

The assumptions of negligible Joule heating and viscous dissipation make the present model particularly suited to moderate electric fields and microscale coating applications. Future studies could extend the model to include strong-field regimes where these effects become non-negligible. The current study has shown that factorial plot analysis and RSM are powerful techniques for optimizing

thermal electro-kinetic coating flows. However, the analysis has been restricted to Newtonian ionic liquids and Fourier heat conduction and has also ignored porous media effects, all of which may arise in thermo-electro-convective coating dynamics. Future studies may consider viscoelastic ionic liquids and non-Fourier heat flux, and also electrolytic nanofluids, chemical reaction, and non-Darcy permeable medium effects.

Acknowledgement: Not applicable.

Funding Statement: The authors received no specific funding for this study.

Author Contributions: Conceptualization, J. Prakash and O. Anwar Bég; Methodology, Dharmendra Tripathi; Software, J. Prakash; Validation, J. Prakash; Formal analysis, S. Kuharat and Kh. S. Mekheimer; Investigation, O. Anwar Bég and S. Kuharat; Data curation, O. Anwar Bég; Visualization, S. Kuharat; Writing—original draft preparation, J. Prakash; Writing—review and editing, Dharmendra Tripathi and Kh. S. Mekheimer; Supervision, Dharmendra Tripathi. All authors reviewed the results and approved the final version of the manuscript.

Availability of Data and Materials: Not applicable.

Ethics Approval: Not applicable.

Conflicts of Interest: The authors declare no conflicts of interest to report regarding the present study.

References

1. Crane LJ. Flow past a stretching plate. J Appl Math Phys. 1970;21(4):645–7. doi:10.1007/bf01587695.
2. Kumaran V, Ramanaiah G. A note on the flow over a stretching sheet. Acta Mech. 1996;116(1):229–33. doi:10.1007/BF01171433.
3. Vajravelu K, Cannon JR. Fluid flow over a nonlinearly stretching sheet. Appl Math Comput. 2006;181(1):609–18. doi:10.1016/j.amc.2005.08.051.
4. Ishak A. Thermal boundary layer flow over a stretching sheet inamicropolar fluid with radiation effect. Meccanica. 2010;45(3):367–73. doi:10.1007/s11012-009-9257-4.
5. Fang T, Zhang J, Zhong Y. Boundary layer flow over a stretching sheet with variable thickness. Appl Math Comput. 2012;218(13):7241–52. doi:10.1016/j.amc.2011.12.094.
6. Rana P, Bhargava R, Bég OA. Finite element simulation of unsteady magneto-hydrodynamic transport phenomena on a stretching sheet in a rotating nanofluid. Proc Inst Mech Eng Part N J Nanoeng Nanosyst. 2013;227(2):77–99. doi:10.1177/1740349912463312.
7. Hassanien IA, Abdullah AA, Gorla RSR. Flow and heat transfer in a power-law fluid over a nonisothermal stretching sheet. Math Comput Model. 1998;28(9):105–16. doi:10.1016/S0895-7177(98)00148-4.
8. Siddheshwar PG, Mahabaleswar US. Effects of radiation and heat source on MHD flow of a viscoelastic liquid and heat transfer over a stretching sheet. Int J Non Linear Mech. 2005;40(6):807–20. doi:10.1016/j.ijnonlinmec.2004.04.006.
9. Jat RN, Chaudhary S. MHD flow and heat transfer over a stretching sheet. Appl Math Sci. 2009;3(26):1285–94.
10. Salleh MZ, Nazar R, Pop I. Boundary layer flow and heat transfer over a stretching sheet with Newtonian heating. J Taiwan Inst Chem Eng. 2010;41(6):651–5. doi:10.1016/j.jtice.2010.01.013.
11. Hayat T, Qasim M, Mesloub S. MHD flow and heat transfer over permeable stretching sheet with slip conditions. Numer Methods Fluids. 2011;66(8):963–75. doi:10.1002/fld.2294.

12. Cortell R. Fluid flow and radiative nonlinear heat transfer over a stretching sheet. J King Saud Univ Sci. 2014;26(2):161–7. doi:10.1016/j.jksus.2013.08.004.
13. Sreedevi P, Sudarsana Reddy P, Chamkha A. Heat and mass transfer analysis of unsteady hybrid nanofluid flow over a stretching sheet with thermal radiation. SN Appl Sci. 2020;2(7):1222. doi:10.1007/s42452-020-3011-x.
14. Chakrabarti A, Gupta AS. Hydromagnetic flow and heat transfer over a stretching sheet. Q Appl Math. 1979;37(1):73–8. doi:10.1090/qam/99636.
15. Andersson HI. An exact solution of the Navier-Stokes equations for magnetohydrodynamic flow. Acta Mech. 1995;113(1):241–4. doi:10.1007/BF01212646.
16. Pop I, Na TY. A note on MHD flow over a stretching permeable surface. Mech Res Commun. 1998;25(3):263–9. doi:10.1016/s0093-6413(98)00037-8.
17. Fang T, Zhang J, Yao S. Slip MHD viscous flow over a stretching sheet-An exact solution. Commun Nonlinear Sci Numer Simul. 2009;14(11):3731–7. doi:10.1016/j.cnsns.2009.02.012.
18. Gnaneswara Reddy M, Tripathi D, Anwar Bég O. Analysis of dissipative non-Newtonian magnetic polymer flow from a curved stretching surface with slip and radiative effects. Heat Transf. 2023;52(3):2694–714. doi:10.1002/htj.22801.
19. Shahid A, Wei W, Bhatti MM, Bég OA, Bég TA. Mixed convection Casson polymeric flow from a nonlinear stretching surface with radiative flux and non-Fourier thermal relaxation effects: computation with CSNIS. ZAMM J Appl Math Mech. 2023;103(10):e202200519. doi:10.1002/zamm.202200519.
20. Tazin T, Ferdows M, Anwar BégO, Bég TA, Kadir A. Computation of stagnation flow of magnetite/cobalt/manganese-zinc-aqueous nano-ferrofluids from a stretching sheet with magnetic induction effects. Int J Comput Methods Eng Sci Mech. 2023;24(6):371–90. doi:10.1080/15502287.2023.2211985.
21. Masliyah JH, Bhattacharjee S. Electrokinetic and colloid transport phenomena. Hoboken, NJ, USA: John Wiley & Sons, Inc.; 2005. doi:10.1002/0471799742.
22. Castellanos A, Ramos A, González A, Green NG, Morgan H. Electrohydrodynamics and dielectrophoresis in microsystems: scaling laws. J Phys D: Appl Phys. 2003;36(20):2584–97. doi:10.1088/0022-3727/36/20/023.
23. Ren L, Escobedo C, Li D. Electroosmotic flow in a microcapillary with one solution displacing another solution. J Colloid Interface Sci. 2001;242(1):264–71. doi:10.1006/jcis.2001.7809.
24. Yang WC, Macka M, Haddad PR. Biopolymer-coated fused silica capillaries for high magnitude cathodic or anodic electro-osmotic flows in capillary electrophoresis. Chromatographia. 2003;57(S1):S187–93. doi:10.1007/bf02492101.
25. Konášová R, Butnariu M, Šolínová V, Kašička V, Koval D. Covalent cationic copolymer coatings allowing tunable electroosmotic flow for optimization of capillary electrophoretic separations. Anal Chim Acta. 2021;1178:338789. doi:10.1016/j.aca.2021.338789.
26. Kasicka V, Prusík Z, Sázelová P, Chiari M, Miksík I, Deyl Z. External electric field control of electroosmotic flow in non-coated and coated fused-silica capillaries and its application for capillary electrophoretic separations of peptides. J Chromatogr B Biomed Sci Appl. 2000;741(1):43–54. doi:10.1016/s0378-4347(00)00076-1.
27. Horvath J, Dolník V. Polymer wall coatings for capillary electrophoresis. Electrophoresis. 2001;22(4):644–55. doi:10.1002/1522-2683(200102)22:4<644::AID-ELPS644>3.0.CO;2-3.
28. Huhn C, Ramautar R, Wuhrer M, Somsen GW. Relevance and use of capillary coatings in capillary electrophoresis-mass spectrometry. Anal Bioanal Chem. 2010;396(1):297–314. doi:10.1007/s00216-009-3193-y.
29. Leclercq L, Morvan M, Koch J, Neusüß C, Cottet H. Modulation of the electroosmotic mobility using polyelectrolyte multilayer coatings for protein analysis by capillary electrophoresis. Anal Chim Acta. 2019;1057:152–61. doi:10.1016/j.aca.2019.01.008.
30. Sola L, Chiari M. Tuning capillary surface properties by charged polymeric coatings. J Chromatogr A. 2015;1414:173–81. doi:10.1016/j.chroma.2015.08.032.

31. Sun P, Landman A, Barker GE, Hartwick RA. Synthesis and evaluation of anionic polymer-coated capillaries with pH-independent electroosmotic flows for capillary electrophoresis. J Chromatogr A. 1994;685(2):303–12. doi:10.1016/0021-9673(94)00635-0.
32. Prakash J, Tripathi D. Study of EDL phenomenon in Peristaltic pumping of a Phan-Thien-Tanner Fluid through asymmetric channel. Korea Aust Rheol J. 2020;32(4):271–85. doi:10.1007/s13367-020-0026-1.
33. Balaji R, Prakash J, Tripathi D, Bég OA. Computation of magnetohydrodynamic electro-osmotic modulated rotating squeezing flow with *Zeta* potential effects. Colloids Surf A Physicochem Eng Aspects. 2022;640(2):128430. doi:10.1016/j.colsurfa.2022.128430.
34. Misra JC, Sinha A. Electro-osmotic flow and heat transfer of a non-Newtonian fluid in a hydrophobic microchannel with Navier slip. J Hydrodyn. 2015;27(5):647–57. doi:10.1016/S1001-6058(15)60527-3.
35. Zhang X, Yang D, Israr Ur Rehman M, Hamid A. Heat transport phenomena for the darcy-forchheimer flow of casson fluid over stretching sheets with electro-osmosis forces and Newtonian heating. Mathematics. 2021;9(19):2525. doi:10.3390/math9192525.
36. Hafez NM, Thabet EN, Khan Z, Abd-Alla AM, Elhag SH. Electroosmosis-modulated Darcy-Forchheimer flow of Casson nanofluid over stretching sheets in the presence of Newtonian heating. Case Stud Therm Eng. 2024;53:103806. doi:10.1016/j.csite.2023.103806.
37. Box GEP, Behnken DW. Some new three level designs for the study of quantitative variables. Technometrics. 1960;2(4):455. doi:10.2307/1266454.
38. Montgomery DC. Design and analysis of experiments. Hoboken, NJ, USA: John Wiley & Sons, Inc.; 2017.
39. Gardiner WP, Gettinby G. Experimental design techniques in statistical practice: a practical software-based approach. Amsterdam, The Netherlands: Elsevier; 1998.
40. Ahmad AL, Low SC, Abd Shukor SR, Ismail A. Optimization of membrane performance by thermal-mechanical stretching process using responses surface methodology (RSM). Sep Purif Technol. 2009;66(1):177–86. doi:10.1016/j.seppur.2008.11.007.
41. Venkatadri K, Öztop HF, Ramachandra PrasadV, Parthiban S, Anwar BégO. RSM-based sensitivity analysis of hybrid nanofluid MHD flow in an enclosure filled with non-Darcy porous medium using the Lattice Boltzmann Method. Numer Heat Transf A. 2024;85(6):875–99. doi:10.1080/10407782.2023.2193708.
42. Qader BS, Supeni EE, Ariffin MKA, Abu Talib AR. RSM approach for modeling and optimization of designing parameters for inclined fins of solar air heater. Renew Energy. 2019;136(2):48–68. doi:10.1016/j.renene.2018.12.099.
43. Mehmood T, Ramzan M, Howari F, Kadry S, Chu YM. Application of response surface methodology on the nanofluid flow over a rotating disk with autocatalytic chemical reaction and entropy generation optimization. Sci Rep. 2021;11(1):4021. doi:10.1038/s41598-021-81755-x.
44. Khuri AI, Mukhopadhyay S. Response surface methodology. Wires Comput Stat. 2010;2(2):128–49. doi:10.1002/wics.73.
45. Giovanni M. Response surface methodology and product optimization. Food Technol. 1983;37:41–5.
46. Babu MJ, Rao YS, Kumar AS, Raju CSK, Shehzad SA, Ambreen T, et al. Squeezed flow of polyethylene glycol and water based hybrid nanofluid over a magnetized sensor surface: a statistical approach. Int Commun Heat Mass Transf. 2022;135(5):106136. doi:10.1016/j.icheatmasstransfer.2022.106136.
47. Yusuf A, Khan SU, Hassan M, Bhatti MM, Öztop HF. Heat transfer optimization of MWCNT-Al_2O_3 hybrid nanofluids under convective and irreversible effects. J Umm Al Qura Univ Appl Sci. 2025;420(4):34. doi:10.1007/s43994-025-00252-3.